

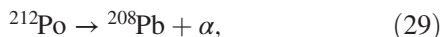
TABLE XI. Decay modes of ^{214}Po .

Decay mode	Branching ratio [%]	Energy [keV]
α	99.99	$E_\alpha = 7833.46$
$\alpha + \gamma$	1.04×10^{-4}	$E_\alpha = 7033.66$ $E_\gamma = 799.7$
$\alpha + \gamma$	6.0×10^{-7}	$E_\alpha = 6735.76$ $E_\gamma = 1097.7$

scintillator offers a possibility to discriminate highly ionizing particles (α , proton) from particles with lower specific ionization (β^- , β^+ , γ) by means of pulse shape analysis. In the case of these rare branches, the scintillation pulses from the α and γ decays are so close in time that they practically overlap and result to be partially α -like. In order to suppress this background to negligible levels, during the purification periods we have increased the lower limit on the charge of delayed signal and applied a slight pulse shape cut as described below in Sec. VII. The final evaluation of the radon correlated background passing the optimized IBD selection cuts will be given in Sec. IX G.

F. $^{212}\text{Bi} - ^{212}\text{Po}$ background

During the WE periods, an increased contamination of ^{220}Rn (^{232}Th chain) was also observed. Among the ^{220}Rn daughters, there is the fast decay sequence of $^{212}\text{Bi}(\beta^-)$ and $^{212}\text{Po}(\alpha)$:



characterized with $\tau = (425.1 \pm 1.5)$ ns of the ^{212}Po decay [123]. The ^{212}Bi is a β^- emitter with $Q = 2.252$ MeV, while the α of ^{212}Po decay has 8.955 MeV energy. Given the short time coincidence, they could be a potential source of background for the IBD candidates, searched among the double cluster events, when both the prompt and delayed fall within one $16 \mu\text{s}$ DAQ gate (Sec. III A). This kind of events was included in the geoneutrino analysis for the first time (Sec. VII B). Fortunately, the ^{212}Po is not giving any $(\alpha + \gamma)$ decay branch, so its effective energy distribution is below the neutron capture peak. Moreover, being a pure α decay, it can be easily recognized and rejected with a proper pulse shape analysis. The final evaluation of this background passing the optimized selection cuts will be given in Sec. IX H.

VII. DATA SELECTION CUTS

In this section we describe the cuts for the selection of antineutrino candidates and the process of their optimization. The vetoes applied after different muon

categories are described in Sec. VII A. Sections VII B and VII C deal with the definitions of the time and spatial correlation windows between the prompt and delayed IBD candidates. The application of the α/β discrimination techniques (Sec. III D) on the delayed, in order to suppress the radon background (Sec. VI E), is shown in Sec. VII D. Optimization of the energy cuts for the prompt and delayed signals is shown in Sec. VII E, while the selection of the dynamic fiducial volume in Sec. VII F. The so-called *multiplicity cut* to suppress the background due to undetected muons with multiple neutrons and some noise is explained in Sec. VII G. Finally, Sec VII H summarizes all the optimized values for all cuts.

A. Muon vetoes

Muons and related spallation products represent an important background for geoneutrino measurement, as described in Sec. VI A. In the data selection, we first remove all categories of detected muons, as defined in Sec. III B. After different types of detected muons, different kinds of vetoes are applied. They are described in this section and are schematically shown in Fig. 23.

1. Veto after external muons

Among different kinds of spallation products of external muons, only cosmogenic neutrons can penetrate inside the scintillator and thus present a background for geoneutrino analysis. The neutron capture time in Borexino is

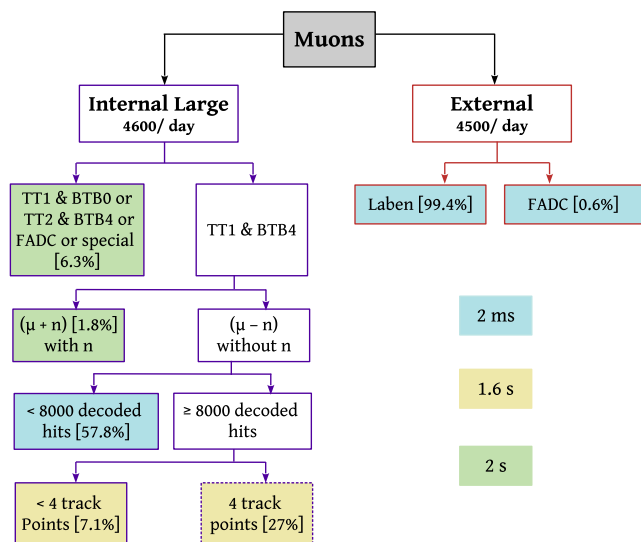


FIG. 23. Scheme of different types of vetoes applied after various muon categories. The relative fraction of each muon category is given by the numbers in brackets. Different colors represent different durations of the time veto. The dashed line around the box at the bottom of the plot represents the only muon category when the cylindrical veto around the muon track is applied. For other categories, the whole detector is vetoed.

$(254.5 \pm 1.8) \mu\text{s}$ [77]. Therefore, a 2 ms veto, i.e., about 8 times the neutron capture time, is applied after all external muons detected by the OD.

2. Veto after internal muons

For internal muons, in addition to fast neutrons, ${}^9\text{Li}$, ${}^8\text{He}$, and ${}^{12}\text{B}$ isotopes (Table IX) are potential background sources for IBD selection as well. In the past analyses, a 2 s veto of the whole detector has been applied after all categories of internal strict and special muons. Since 2 s is nearly 8 times the lifetime of the longest-lived isotope (${}^9\text{Li}$), this background was effectively eliminated for the price of about 10%–11% loss of exposure. In this analysis, we reduce the exposure loss to 2.2% by introducing different categories of vetoes.

(i) 2 s veto of the whole detector

We apply a conservative 2 s veto of the whole detector after internal strict muons, special muons, and FADC muons that did not trigger the OD (not tagged by MTF flag). These represent 6.3% of all internal large muon category, which includes some noise events as well (Sec. III B). In addition, we apply this kind of veto after the so-called $(\mu + n)$ muons, i.e., those internal muons that triggered the OD (*TT1* & *BTB4*, Sec. III A) and were followed by at least one neutron observed in the following event of *TT128*. These muons represent only 1.8% of all internal muons and have a higher probability to produce ${}^9\text{Li}$ events with a detectable decay neutron. The $(\mu + n)$ muon sample was used to characterize the veto parameters after the independent sample of $(\mu - n)$ muons, i.e., MTF/BTB4 internal muons that are not followed by any neutron, as described below.

(ii) 2 ms veto of the whole detector

It was observed that $(\mu + n)$ muons that also produce IBD-like hadronic background, always have more than 8000 decoded hits (Fig. 24). In the following text, we apply the notation $(\mu + n)_{\geq 8000}$ for this and similar muon types. Muons producing less than 8000 decoded hits are typically not crossing the scintillator and are passing only through the buffer, where neutrons cannot be effectively detected due to low light yield. Thus, $(\mu - n)_{< 8000}$ have little chance to produce ${}^9\text{Li}$ events with a detectable decay neutron. We apply a conservative 2 ms dead time after them, suppressing potential fast neutrons with negligible exposure loss. These muons represent 57.8% of all internal muons.

(iii) 1.6 s veto of the whole detector

Muons passing through the scintillator, i.e., with ≥ 8000 decoded hits, have high probability that neutron from a potential ${}^9\text{Li}$ decay would be detected. Thus, for these muons, a 2 ms veto is not sufficient. For the $(\mu - n)_{\geq 8000}$ muon category that

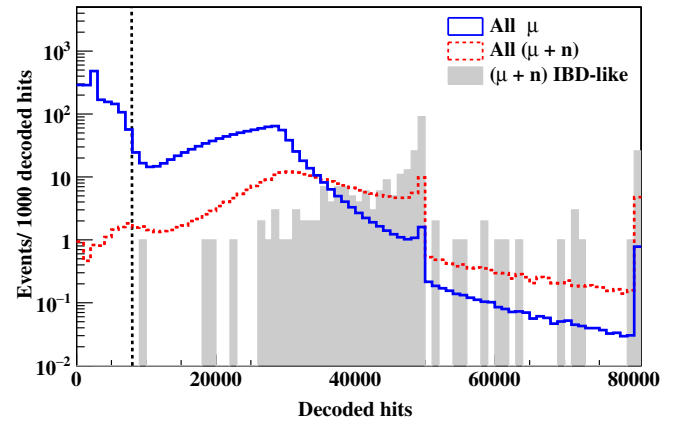


FIG. 24. Comparison of the decoded hits spectra of all the muons (solid blue line), all $(\mu + n)$ muons (dotted red line), and those $(\mu + n)$ muons, which produce IBD-like candidates due to hadronic background within 2 s after muons (filled grey area). The dashed vertical line shows 8000 decoded hits threshold used in the definition of the veto duration. Spectra of all and $(\mu + n)$ muons are normalized to the number of $(\mu + n)$ muons producing IBD-like candidates.

represents 34.1% of all internal muons, we apply a veto reduced from 2 s to 1.6 s, after which only 0.2% of ${}^9\text{Li}$ candidates survive. In addition, only 10% of the observed ${}^9\text{Li}$ background is produced due to $(\mu - n)_{\geq 8000}$ muons, as it will be explained in detail in Sec. IX C.

Muons in Borexino can be tracked based on their reconstructed entry and exit points in the OD and ID [77]. We consider the muon track to be reliable only when all the four track points are reconstructed. When this is not the case, the 1.6 s veto is applied to the whole detector, for 7.1% of all internal muons.

(iv) 1.6 s cylindrical veto

The application of a cylindrical veto around the muon track, as schematically shown in Fig. 25(a), instead of vetoing the whole detector, can further increase the exposure for geoneutrino analysis. This kind of veto is applied to $(\mu - n)_{\geq 8000}$ muons for which all the four muon track points are reconstructed.

The radius of the cylindrical veto is set by studying the lateral distance between the muon and IBD-like prompt and delayed observed within 2 s after the passage of a $(\mu + n)$ muon with four track points (Fig. 25(b)). Within the observed statistics, this distance is very similar for the prompt and the delayed. 97.7% of the prompts (on which the DFV cut is applied) lie within a 3 m radius from the muon track in the IBD selection (Sec. VII F). Since the lateral distribution of the muon daughters is expected to be the same for $(\mu - n)$ muons as well, a cylindrical veto of 1.6 s duration with 3 m radius is applied for $(\mu - n)_{\geq 8000}$ muons, which constitute 27% of all internal muons.

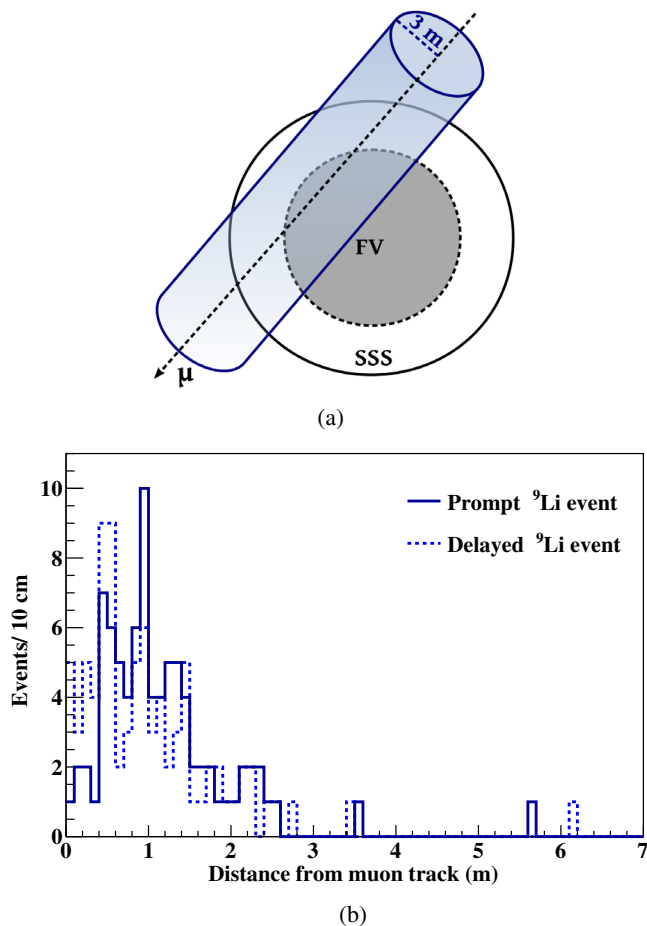


FIG. 25. Top (a): A schematic representation of the cylindrical veto applied around the muon track for 1.6 s after the $(\mu - n)_{\geq 8000}$ muons with reliable track reconstruction. Bottom (b): Distributions of the distances of 85 ⁹Li IBD-like events from reliably reconstructed tracks of $(\mu + n)$ muons: solid and dashed lines represent the prompt and delayed candidates, respectively.

The resulting exposure loss of 2.2% after all muon vetoes was calculated using a Monte Carlo simulation. In total, 74 million pointlike events were generated homogeneously in the dynamical fiducial volume for this study (Sec. VII F), following the changing shape of the IV (Sec. III C). After considering the GPS times of all the muons and the track geometry reconstructed for $(\mu - n)_{\geq 8000}$ muons, the relative exposure loss was calculated as the fraction of the events removed by all vetoes.

B. Time coincidence

The coincidence time window between the prompt and the delayed (dt) is an important background-suppressing cut. It is implemented based on the neutron capture time that was measured during the calibration campaign with the ²⁴¹Am – ⁹Be neutron source to be $(254.5 \pm 1.8) \mu\text{s}$ [77]. Considering the 16 μs DAQ window, followed by an

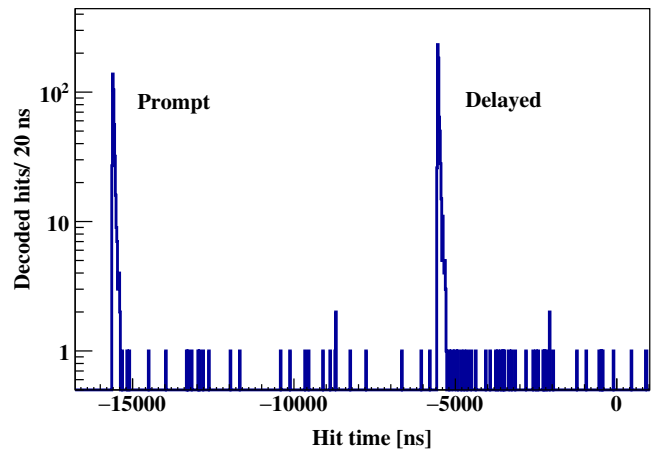


FIG. 26. Example of an IBD candidate, when both the prompt and the delayed are individual clusters in a single event of 16 μs DAQ time window. The negative hit times are expressed with respect to the trigger reference time.

electronics dead time of 2 – 3 μs (Sec. III A), one has to consider separately the case when the prompt and delayed are either two separate events/triggers with single cluster each (similar to the event in top left of Fig. 4), or are represented by two clusters in a single event, as shown in Fig. 26.

1. Single cluster events

For this category of IBD candidates, the coincidence time window is between $dt_{\min} = 20 \mu\text{s}$ and $dt_{\max} = 1280 \mu\text{s}$. The lower threshold guarantees that the delayed signal can trigger after the dead-time of the prompt trigger. The dt_{\max} corresponds to about five times the measured neutron capture time. This time window covers 91.8% of all IBD interactions.

2. Double cluster events

This category of IBD candidates is included in the present analysis for the first time. In this case, the coincidence time window is between $dt_{\min} = 2.5 \mu\text{s}$ and $dt_{\max} = 12.5 \mu\text{s}$. The inclusion of double cluster events led to a 3.8% increase in the IBD tagging efficiency.

The lower threshold was optimized by studying the cluster duration of prompts from the MC of reactor antineutrinos (Sec. VIII), which spectrum extends up to about 10 MeV. It guarantees that even for the highest energy prompt, after the dt_{\min} , there is no light that could alter the hit pattern of the delayed.

The dt_{\max} was set considering the variable position of the trigger-generating cluster (prompt) inside the DAQ window, that occurred during the analyzed period due to the changes in the trigger system. At the same time, it guarantees that the delayed can always have cluster duration of up to 2.5 μs before the end of the DAQ window.

C. Space correlation

Similar to dt , the spatial distance between the prompt and the delayed (dR) is also an important background-suppressing cut. In the previous analyses, $dR = 1$ m was used. The reconstructed distance between the prompt and the delayed is larger with respect to the distance between their respective points of production. This is caused predominantly by these effects:

- (i) *Interaction of gammas*: the gammas, from the positron annihilation and the neutron capture, interact in the LS mostly through several Compton scatterings. Thus, their interaction is intrinsically not pointlike and the barycenter of the cloud of these Compton electrons is not identical to the point of the generation of the gammas.
- (ii) *Position reconstruction*: the position reconstruction (10 cm at 1 MeV) further smears the reconstructed positions.

In the optimization of the dR cut, two main aspects have to be considered. On one hand, in the prompt-delayed reconstructed distance, shown in Fig. 27 for the MC sample of geoneutrinos (Sec. VIII), the efficiency is quickly dropping below 1 m. On the other hand, with the increasing dR , the accidental background is also strongly increasing (Fig. 28). In order to find the optimized value, we have generated thousands of MC pseudoexperiments as described in Sec. X. The cuts were set to optimized values, while the dR cut was varied. The dR cut was then set to 1.3 m, within the interval, where the variation in the expected statistical uncertainty of the geoneutrino measurement is small, as shown in Fig. 28. We note that the procedure of the so-called “sensitivity study” used to estimate the expected statistical uncertainty is described in Sec. X B.

D. Pulse shape discrimination

In the previous geoneutrino analyses, a Gatti cut $G < 0.015$ was applied on the delayed for efficient rejection

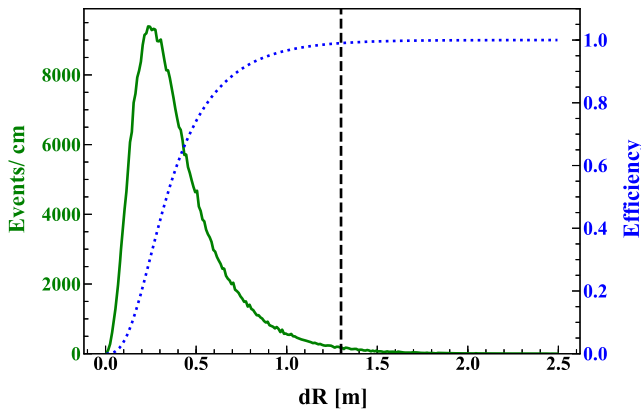


FIG. 27. Distribution of the prompt-delayed reconstructed distance dR (solid green line) shown for the geoneutrino MC sample and the corresponding efficiency (blue dotted line). The vertical dashed line shows the optimized dR cut at 1.3 m.

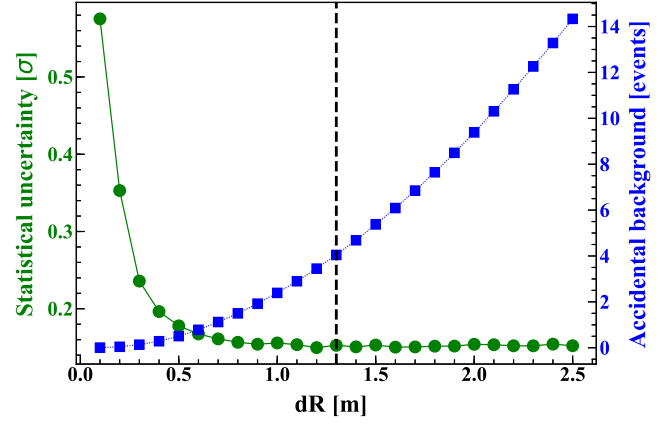


FIG. 28. The expected statistical uncertainty of the geoneutrino measurement using the MC study (filled green circles) and the accidental background (filled blue squares) for different values of dR cut, while the other cuts were set to the optimized values. The vertical dashed line shows the selected value for the dR cut at 1.3 m.

of α -like events from radon-correlated background (Sec. VI E). The cut value was set using gammas from neutron-captures from the $^{241}\text{Am} - ^9\text{Be}$ calibration source and cross checked with the MC. In this analysis, an MLP cut > 0.8 was applied to the delayed using the better α/β discrimination power of the MLP (Sec. III D) when compared to the Gatti. The cut threshold was chosen based on the $^{241}\text{Am} - ^9\text{Be}$ calibration data as shown in Fig. 29. It was found that only a $5.4(8.1) \times 10^{-3}$ fraction of the neutron-capture γ s remains below the MLP threshold of 0.8 for the source position in the detector’s center (close to IV border).”

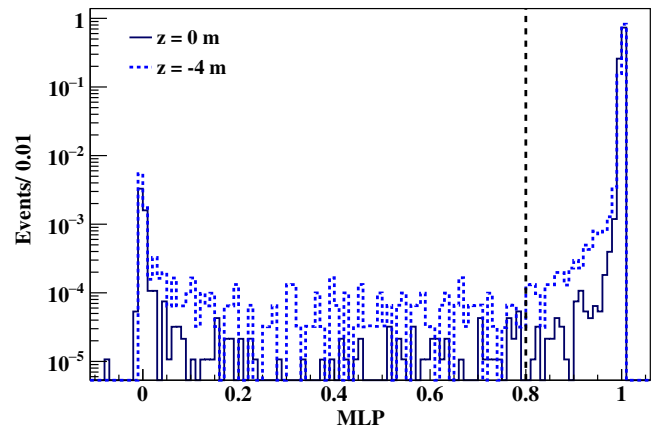


FIG. 29. Distribution of the MLP α/β discriminator (Sec. III D) for the gammas from the capture of neutrons from $^{241}\text{Am} - ^9\text{Be}$ calibration source placed at the detector center $(x, y, z) = (0, 0, 0)$ m, as well as at $(0, 0, -4)$ m, where the observed distribution is the broadest. The dashed line shows the threshold set at 0.8 for the delayed in IBD search.

E. Energy cuts

Energy cuts were applied to the prompt and delayed to aid the identification of IBD signals. The analysis was performed using the charge energy estimator N_{pe} (Sec. III A). The intervals in the respective charges Q_p and Q_d are optimized as explained in this section.

1. Charge of prompt signal

The energy spectrum of the prompt E_p starts at ~ 1 MeV, which corresponds only to the two 511 keV annihilation gammas [Eq. (10)]. Therefore, the threshold on the prompt charge was set to $Q_p^{\min} = 408$ p.e. This threshold value corresponds to approximately 0.8 MeV and remains unchanged from previous analyses. No upper limit is set on the charge of the prompt candidate.

2. Charge of delayed

The delayed signal can be either due to a 2.22 MeV (n -capture on ^1H), or a 4.95 MeV gamma (n -capture on ^{12}C) with about 1.1% probability, as described in Sec. IV. The corresponding values in the N_{pe} variable are 1090 p.e. and 2400 p.e., respectively, as measured in the detector center and shown in Fig. 13. However, at large radii, gammas can partially deposit their energy in the buffer, which decreases the visible energy. Consequently, the γ -peak develops a low-energy tail and even the peak position can shift to lower values (Fig. 30).

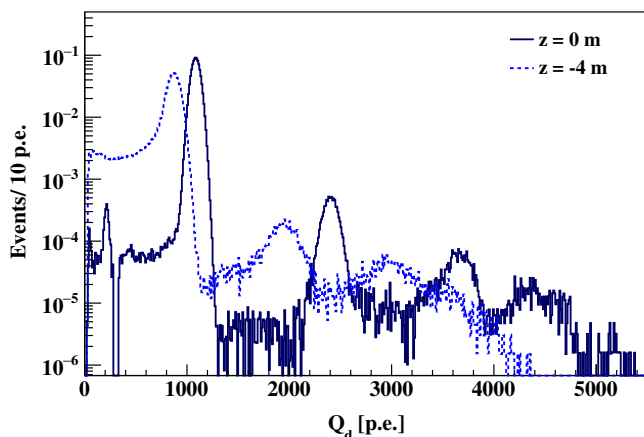


FIG. 30. The N_{pe} spectrum of delayed candidates from the $^{241}\text{Am} - ^9\text{Be}$ calibration source placed at $(x, y, z) = (0, 0, -4)$ m inside the detector (dashed line) compared to the spectrum for the source placed at the detector's center (solid line). The two peaks from the left correspond to 2.2 MeV and 4.95 MeV gammas from neutron captures on ^1H and ^{12}C nuclei, respectively, while the higher energy peaks are from neutron captures on stainless steel nuclei (Fe, Ni, Cr) used in the source construction. All gamma peaks in the off-center spectrum are shifted to lower energies and develop tails due to the partial energy deposits in the buffer. The spectra are normalized to one.

In the last geoneutrino analysis [18], Q_d^{\min} was set to 860 p.e., a conservatively large value because of the radon-correlated background, particularly due to $^{214}\text{Po}(\alpha + \gamma)$ decays. This was discussed in Sec. VI E. In this analysis, Q_d^{\min} was decreased to 700 p.e. based on the improved performance of α/β separation with MLP (Sec. VII D), which improved the ability to suppress $^{214}\text{Po}(\alpha + \gamma)$ decays. This cut was applied to all data with the exception of the water-extraction period, which had an increased radon contamination. In this case the Q_d^{\min} 860 p.e. was retained. The Q_d^{\min} cut was not decreased below 700 p.e. for the following reasons:

- (1) The N_{pe} spectrum of accidental background increases at lower energies, as shown in Fig. 37.
- (2) The endpoint of the α peak from the main ^{214}Po decay in the radon-correlated background is ~ 600 p.e., as described in Sec. IX G.

In this analysis, we include the neutron captures on ^{12}C (4.95 MeV) as well. Consequently, Q_d^{\max} was increased from 1300 p.e. (2.6 MeV) to 3000 p.e. (≈ 5.5 MeV).

F. Dynamical fiducial volume cut

The shape of the Borexino IV, that is changing due to the presence of a small leak, can be periodically reconstructed by using the data (Sec. III C). A DFV cut, i.e., a requirement of some minimal distance of the prompt from the IV, d_{IV} , is applied along the reconstructed IV shape. In the previous analysis [18] a conservative cut of $d_{IV} = 30$ cm has been applied to account for the uncertainty of the IV shape reconstruction and the potential background coincidences near the IV. In this analysis, the DFV was increased by using $d_{IV} = 10$ cm, which leads to a 15.8% relative increase in exposure. This choice is justified below.

The geoneutrino sensitivity studies (Sec. X) were performed for different combinations of the DFV cut and the Q_d^{\min} , as shown in Fig. 31. The choice of Q_d^{\min} does not have a big impact on the expected precision, for a given DFV cut. Order of 5% improvement in the statistical uncertainty of the geoneutrino measurement is expected when the cut is lowered to $d_{IV} = 10$ cm, while there is no further improvement when no DFV cut is applied. A $d_{IV} = 10$ cm DFV cut is also sufficient to account for the precision of the IV shape reconstruction (Sec. III C). In addition, we have verified that no excess of the IBD candidates is observed at large radii (close to the IV), as it will be shown in Sec. XI A.

G. Multiplicity cut

The *multiplicity cut* requires that no additional “high-energy” ($N_{pe} > 400$ p.e.) event is observed within ± 2 ms around either the prompt or the delayed candidate. This cut is designed to suppress the background from undetected muons, for example, neutron-neutron or buffer muon-neutron pairs. This justifies the selected time window

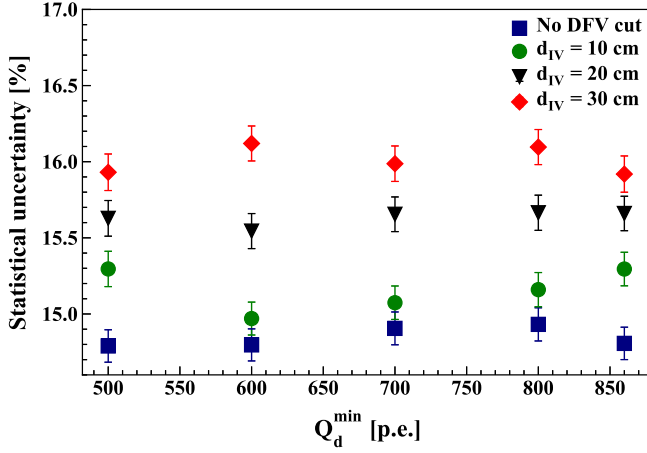


FIG. 31. The expected precision of the geoneutrino measurement for different DFV cuts. For a given DFV cut, the choice of Q_d^{\min} , shown on the x -axis, does not strongly influence the geoneutrino expected precision. Also note, that for $d_{IV} = 10$ cm (final choice) and no DFV cut, the sensitivity to geoneutrinos is nearly the same.

which is nearly 8 times the neutron capture time. The charge cut was lowered to account for those neutrons that are depositing their energy partially in the buffer. Thanks to a high radiopurity of the LS, the corresponding exposure loss due to accidental coincidences of IBD candidates with $N_{pe} > 400$ p.e. events within 2 ms is of the order of 0.01%, which is negligible.

H. Summary of the selection cuts

The summary of all the optimized selection cuts is listed in Table XII.

TABLE XII. Summary of the optimized selection cuts for IBD candidates: charge cut on the prompt, Q_p and delayed, Q_d , time and space correlation dt and dR , respectively, distance to the IV, d_{IV} , MLP α/β particle identification parameter cut on delayed, and multiplicity cut. The scheme indicating the duration and geometry of the different muon vetoes is shown in Fig. 23.

Cut	Condition
Q_p	>408 p.e.
Q_d	(700–3000) p.e. (860–3000) p.e. (WE period)
dt	Double cluster: (2.5–12.5) μ s Single cluster: (20–1280) μ s
dR	1.3 m
Muon veto	2 s or 1.6 s or 2 ms (internal μ) 2 ms (external μ)
d_{IV}	10 cm (prompt)
PID (α/β)	MLP $_d > 0.8$
Multiplicity	No $N_{pe} > 400$ p.e. event ± 2 ms around prompt/delayed

VIII. MONTE CARLO OF SIGNAL AND BACKGROUNDS

The spectral fit of the prompt charge Q_p (Sec. X A), relies extensively on the use of MC-constructed probability distribution functions (PDFs) which represent the shapes of geoneutrino signal and, with the exception of accidental coincidences (Sec. IX D), all backgrounds. The construction of these PDFs is described in Sec. VIII A. The GEANT4 based MC of the Borexino detector was tuned on independent data acquired during an extensive calibration campaign with radioactive sources [76] and is described in detail in [27]. For the antineutrino analysis, the calibration with $^{241}\text{Am} - ^9\text{Be}$ neutron source is of particular importance, since the delayed IBD (Sec. IV) signal is represented by a neutron. The comparison of the neutron spectra from the $^{241}\text{Am} - ^9\text{Be}$ calibration source at the detector center and at (0, 0, -4) m position inside the detector is shown in Fig. 30.

A. Monte Carlo spectral shapes

Once the full *G4Bx2* MC code is working reliably and the origin of the signal and backgrounds is known, it is, in principle, easy to simulate the PDFs that incorporate the detector response and that can be used directly in the spectral fit (Sec. X A).

The simulated signal and backgrounds follow the same experimental conditions as observed in real data, including the number of working channels, the shape of the IV, and the dark noise, as described in [27]. Each run of the complete dataset from December 2007 to April 2019 is simulated individually. After the simulation, the optimized geoneutrino selection cuts (Sec. VII H) are applied as in the real data.

For antineutrinos, pairs of positrons and neutrons were simulated. The neutron energy spectrum is taken from [124], while for the positrons the energy spectra as discussed in Sec. V are used. The antineutrino energy spectra are transformed to positron energy spectra following Eq. (10). In particular, for geoneutrinos, the energy spectra as in Fig. 18 are used. Individual spectra from ^{232}Th and ^{238}U chains were also simulated, so that they can be weighted according to the expected R_s ratio (Eq. (18) for different geological contributions. For reactor antineutrinos, calculated energy spectra “with and without 5 MeV excess” as in Fig. 19 are used as MC input. The resulting PDFs are shown in Fig. 32.

The MC-based PDFs for nonantineutrino backgrounds are shown in Fig. 33. A dedicated code is developed within the *G4Bx2* simulation framework for the generation of ^9Li events, based on Nuclear Data Tables and literature data [125]. The input for (α, n) background simulation is discussed in Sec. VIC, while for atmospheric neutrinos in Sec. VD.

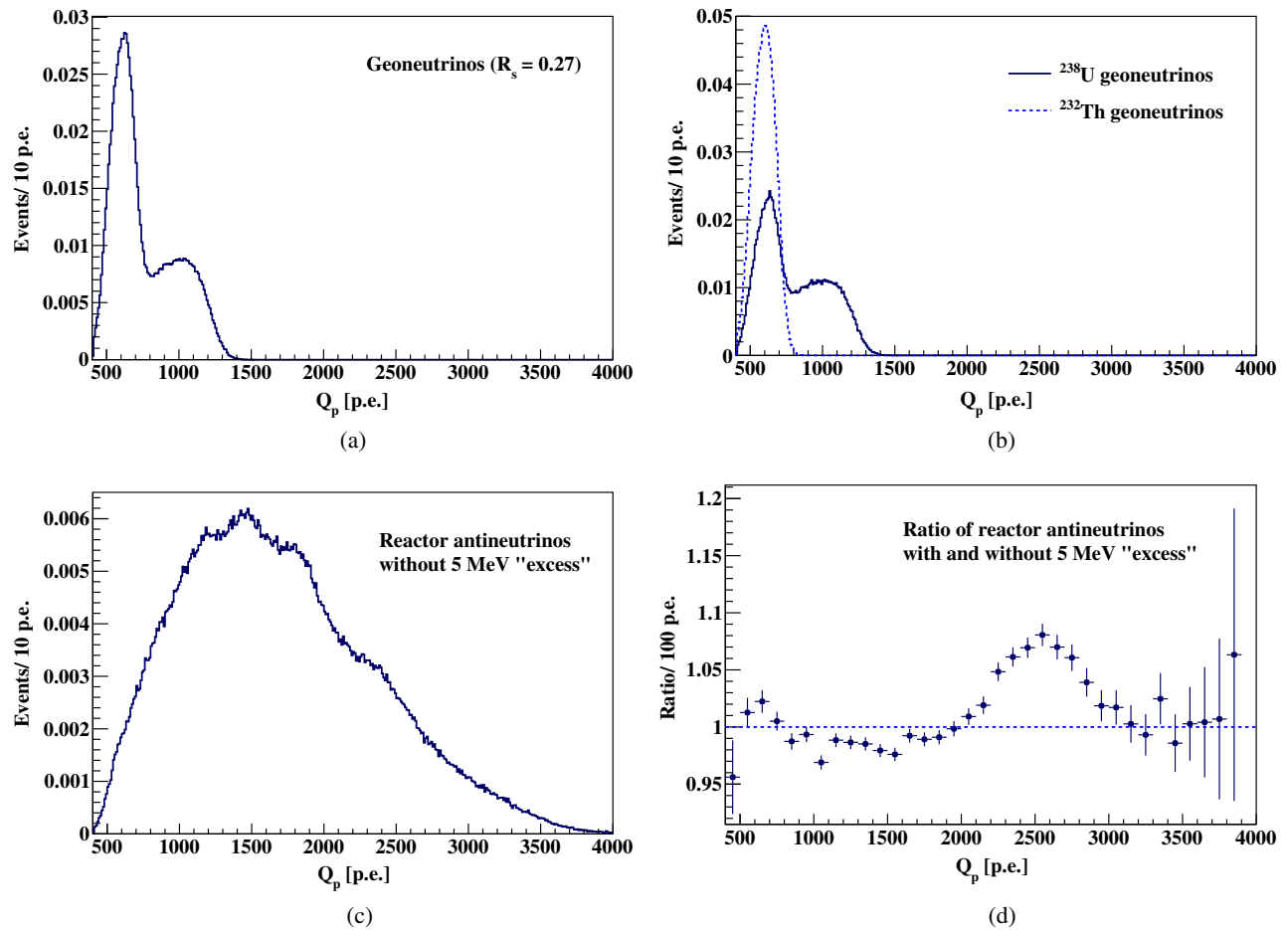


FIG. 32. The MC-based PDFs normalized to one, i.e., the expected shapes of prompts for geoneutrinos and reactor antineutrinos, after optimized geoneutrino selection cuts, that include the detector response. Top-left: geoneutrinos with Th/U ratio fixed to the chondritic value ($R_S = 0.27$). Top-right: ^{238}U and ^{232}Th PDFs shown separately. Bottom-left: reactor antineutrinos “without 5 MeV excess.” Bottom-right: ratio of reactor antineutrino spectra “with/without 5 MeV excess” (Sec. V C), normalized to the same number of events each, in order to demonstrate the difference in shape only.

The PDFs of prompts due to antineutrinos from a hypothetical georeactor (Sec. V E) are shown in Fig. 34. We compare the shapes (in all cases normalized to one) for the non-oscillated spectrum and for the oscillated cases with the georeactor placed at three different positions GR1, GR2, and GR3 as shown in Fig. 21(a). As it can be seen, the shapes of the prompt energy spectra are almost identical.

B. Detection efficiency

The detection efficiencies for geoneutrinos (ϵ_{geo} , ϵ_{Th} , ϵ_{U}), reactor antineutrinos (ϵ_{rea}), and antineutrinos from a hypothetical georeactor (ϵ_{georea}) are summarized in Table XIII. They represent a fraction of MC events passing all the optimized data selection cuts (Sec. VII H) from those generated in the FV of this analysis (10 cm DFV cut). The errors due to the FV definition and the position reconstruction resolution are included in the calculation of the systematic uncertainty, as it will be discussed in

Sec. XIC. The error on the detection efficiency was estimated based on the comparison of the calibration data (most importantly $^{241}\text{Am} - ^9\text{Be}$ neutron source data) with MC simulation. The major contribution comes from the uncertainties of the detector response close to the edge of IV.

IX. EVALUATION OF THE EXPECTED SIGNAL AND BACKGROUNDS WITH OPTIMIZED CUTS

In this section the evaluation of the number of expected antineutrino signal and background events after the optimized selection cuts (Table XII) is described. The dataset and the total exposure are presented in Sec. IX A. The number of expected antineutrino events from different sources, based on the estimated antineutrino signals as in Table VIII, is presented in Sec. IX B. The next sections treat the nonantineutrino background, following the structure of Sec. VI, where the physics of each of these

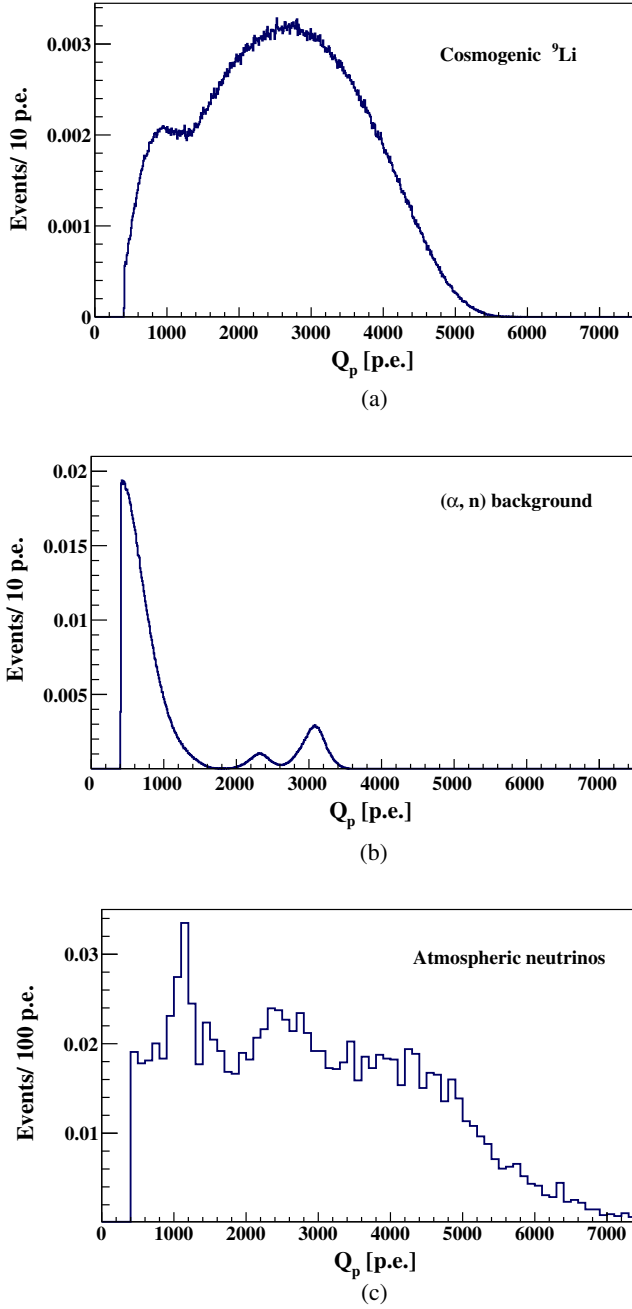


FIG. 33. MC-based PDFs of prompts for different backgrounds after optimized geoneutrino selection cuts, normalized to one. Top: cosmogenic ${}^9\text{Li}$ background. Middle: (α, n) background. Bottom: atmospheric neutrino background.

background categories is described. In particular, cosmogenic background is discussed in Sec. IX C, accidental background in Sec. IX D, (α, n) interactions in Sec. IX E, (γ, n) and fission in PMTs in Sec. IX F, radon correlated background in Sec. IX G, and finally ${}^{212}\text{Bi} - {}^{212}\text{Po}$ background in Sec. IX H. Section IX I summarizes the expected total number of nonantineutrino background events.

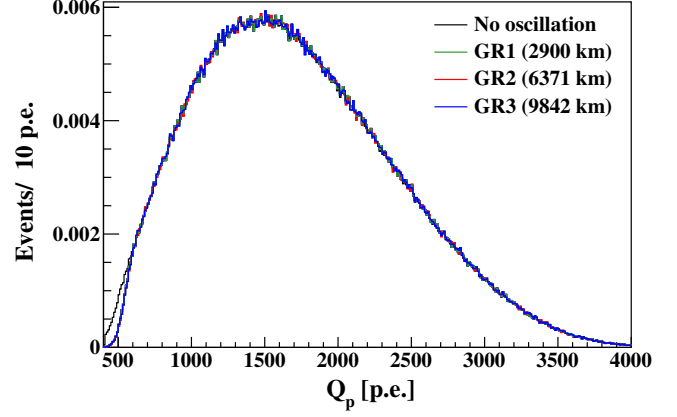


FIG. 34. MC-based PDFs of prompts for a georeactor (Sec. V E) after optimized IBD selection cuts, normalized to one. We show both the case of nonoscillated spectrum, as well as the oscillated spectra for the georeactor placed in three positions at different depths: GR1 ($d = 2900$ km), GR2 ($d = 6371$ km), and GR3 ($d = 9842$ km), defined in Fig. 21(a).

A. Data set and exposure

In this analysis the data taken between December 9, 2007 and April 28, 2019, corresponding to $t_{\text{DAQ}} = 3262.74$ days of data taking, are considered. The average life-time weighted IV volume and the FV used in this analysis (DFV cut $d_{\text{IV}} = 10$ cm) are $\bar{V}_{\text{IV}} = (301.3 \pm 10.9) \text{ m}^3$ and $\bar{V}_{\text{FV}} = (280.1 \pm 10.1) \text{ m}^3$, respectively, after taking the changing shape of the IV into account (Sec. III C). These correspond to the average IV and FV mass of $\bar{m}_{\text{IV}} = (264.5 \pm 9.6) \text{ ton}$ and $\bar{m}_{\text{FV}} = (245.8 \pm 8.7) \text{ ton}$, respectively, considering the scintillator density of $\rho_{\text{LS}} = (0.878 \pm 0.004) \text{ g cm}^{-3}$. The total exposure after the cosmogenic veto (Sec. VII A) and in the FV is $\mathcal{E} = (2145.8 \pm 82.1) \text{ ton} \times \text{yr}$, considering the systematic uncertainty on position reconstruction (Sec. XI C). This can be expressed as $\mathcal{E}_p = (1.29 \pm 0.05) \times 10^{32} \text{ protons} \times \text{yr}$, using the proton density in Borexino

TABLE XIII. Detection efficiencies after the optimized selection cuts for geoneutrinos from ${}^{238}\text{U}$ and ${}^{232}\text{Th}$ chains individually and for their summed contribution (according to the chondritic Th/U mass ratio), as well as for antineutrinos from reactors and from a hypothetical georeactor. The efficiencies were determined based on the MC simulation of each component. The error is estimated using the calibration data.

Source	Efficiency [%]
${}^{238}\text{U}$ geoneutrinos	87.6 ± 1.5
${}^{232}\text{Th}$ geoneutrinos	84.8 ± 1.5
Geoneutrinos ($R_s = 0.27$)	87.0 ± 1.5
Reactor antineutrinos	89.5 ± 1.5
Georeactor	89.6 ± 1.5

LS of $N_p = (6.007 \pm 0.001) \times 10^{28}$ protons ton^{-1} . Applying the geoneutrino detection efficiency described in Sec. VIII B, the effective exposure for the geoneutrino detection reduces to $\mathcal{E}' = (1866.4 \pm 78.4) \text{ ton} \times \text{yr}$ and $\mathcal{E}'_p = (1.12 \pm 0.05) \times 10^{32}$ protons $\times \text{yr}$.

B. Antineutrino events

This section summarizes the number of expected antineutrino events detected with the optimized selection cuts, assuming the expected antineutrino signals as given in Table VIII. An overview is given in Table XIV.

C. Cosmogenic background

The various cosmogenic backgrounds in Borexino which affect the geoneutrino analysis were explained in Sec. VI A, while the analysis and technical evaluation of these backgrounds is explained in this section.

TABLE XIV. Summary of the expected number of antineutrino events with optimized selection cuts in the geoneutrino (408–1500) p.e and reactor antineutrino (408–4000) p.e. energy ranges. The errors include uncertainties on the predicted signal only. The reference exposure $\mathcal{E}_p = (1.29 \pm 0.05) \times 10^{32}$ protons $\times \text{yr}$ corresponds to the analyzed period.

Model	Energy range [p.e.]	Signal [Events]
Geoneutrinos		
Bulk lithosphere	408–1500	$28.8^{+5.5}_{-4.6}$
CC BSE (total)	408–1500	$31.9^{+6.2}_{-5.4}$
CC BSE (mantle)	408–1500	2.8 ± 0.6
GC BSE (total)	408–1500	$38.8^{+6.2}_{-5.4}$
GC BSE (mantle)	408–1500	9.8 ± 0.9
GD BSE (total)	408–1500	$51.1^{+6.3}_{-5.5}$
GD BSE (mantle)	408–1500	22.0 ± 1.2
FR (total)	408–1500	$62.0^{+6.4}_{-5.6}$
FR (mantle)	408–1500	33.0 ± 1.7
Reactor antineutrinos		
without	408–1500	42.6 ± 0.7
“5 MeV excess”	408–4000	$97.6^{+1.7}_{-1.6}$
with	408–1500	39.5 ± 0.7
“5 MeV excess”	408–4000	$91.9^{+1.6}_{-1.5}$
Atmospheric neutrinos		
	408–1500	2.2 ± 1.1
	408–4000	3.3 ± 1.6
	408–8000	9.2 ± 4.6
1 TW Georeactor		
GR2: Earth’s center	408–1500	3.6 ± 0.1
	408–4000	8.9 ± 0.3
GR1: CMB at 2900 km	408–1500	17.6 ± 0.5
	408–4000	43.1 ± 1.3
GR3: CMB at 9842 km	408–1500	1.5 ± 0.04
	408–4000	3.7 ± 0.1

1. Hadronic background

The hadronic background, expected to be dominated by ${}^9\text{Li}$ (Sec. VII A), which remains after the detected muons out of the vetoed space and time is evaluated here. We first study the time and spatial distributions of the detected ${}^9\text{Li}$ candidates with respect to the parent muon. After that, this background is evaluated for the different kinds of internal muons according to the respective vetoes applied after them, as previously described in Sec. VII A and summarized in Fig. 23.

a. Time distribution $dt_{\text{Li}-\mu}$.—First, a search for IBD-like signals, passing the optimized selection cuts (Table XII), is performed after the category of muons for which 1.6 or 2.0 s veto is applied. We perform this search starting from 2 ms after each muon, in order to remove cosmogenic neutrons. In total, we found 305 such IBD-like candidates, dominated by 282 candidates after $(\mu + n)$ muons. The Q_p^{Li} charge energy spectrum of the prompts is compatible with the expected MC spectrum of ${}^9\text{Li}$, as it is shown in Fig. 35(a). The distribution of the time differences between the prompt and the preceding muon, $dt_{\text{Li}-\mu}$, is shown in Fig. 35(b). As it can be seen, no events are observed after $dt_{\text{Li}-\mu} > 1.6$ s. The decay time τ is extracted by performing an exponential fit to the $dt_{\text{Li}-\mu}$ distribution and is found to be (0.260 ± 0.021) s. This is compatible with $\tau_{{}^9\text{Li}} = 0.257$ s decay time of ${}^9\text{Li}$.

b. Spatial distribution $dR_{\text{Li}-\mu}$.—The distance of the ${}^9\text{Li}$ prompt from the muon track, $dR_{\text{Li}-\mu}$, is studied for $(\mu + n)$ muons with reliably reconstructed tracks. It is shown for 85 candidates in Fig. 35(c). This distribution is fit with the convolution of an exponential (with a characteristic length λ) with a Gaussian with parameters μ and σ , and a normalization factor n :

$$f(dR_{\text{Li}-\mu}; \lambda, \sigma, \mu, n) = \frac{n}{2\lambda} \times \exp\left(\frac{2\mu + \sigma^2\lambda^{-1} - 2dR_{\text{Li}-\mu}}{2\lambda}\right) \times \text{erfc}\left(\frac{\mu + \sigma^2\lambda^{-1} - dR_{\text{Li}-\mu}}{\sqrt{2}\sigma}\right). \quad (30)$$

The fit results in $\sigma = (0.35 \pm 0.11)$ m, which represents well the combined position reconstruction of the muon track and the prompt, and in $\lambda = (0.68 \pm 0.24)$ m. Considering these values and the fit function in Eq. (30), 2.75% of ${}^9\text{Li}$ prompts would be reconstructed out of the cylinder with 3.0 m radius around the muon track. Below, the hadronic background after different muon-veto categories (Fig. 23) is evaluated, considering the $dt_{\text{Li}-\mu}$ and $dR_{\text{Li}-\mu}$ parametrizations described above.

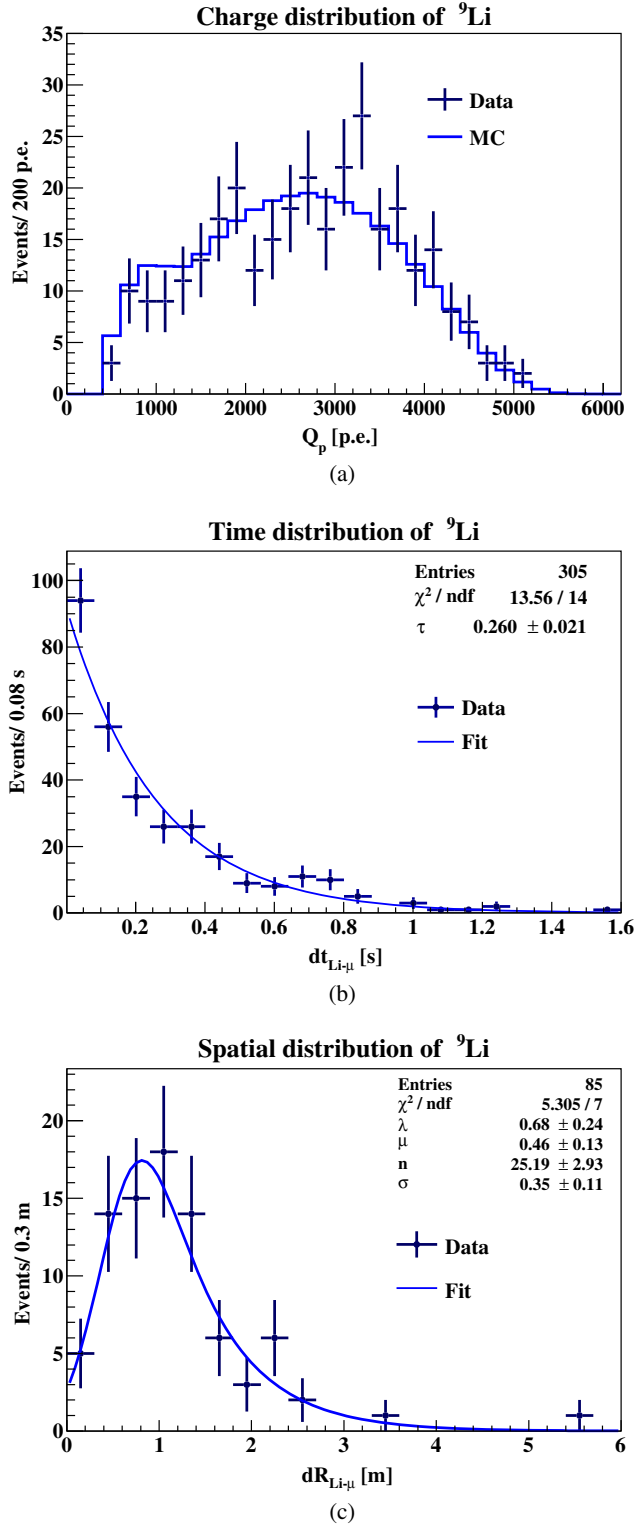


FIG. 35. Distributions of the observed ${}^9\text{Li}$ cosmogenic background, i.e., the IBD-like candidates after optimized selection cuts following muons after at least 2 ms. (a) Comparison of the prompt Q_p^{Li} charge data spectra (points) with the MC spectrum (solid line). (b) Distribution of $dt_{\text{Li}-\mu}$, the time difference between the prompt and the preceding muon, fit with the exponential function. (c) Distribution of $dR_{\text{Li}-\mu}$, the distance of the prompt from the well reconstructed muon track, fit with the function in Eq. (30).

(i) *1.6 s and 2.0 s vetoes of the whole detector:*

For 8.1(7.1)% of the total muons, we veto the whole detector for 1.6(2.0) s. In the time window [2 ms, 1.6(2.0) s] after these muons, where IBD-like candidates were searched, falls 99.02(99.19)% of the corresponding ${}^9\text{Li}$ background. In this window, 282(23) candidates were found. Finally, in the time window after the time veto, the remaining background is $\exp(-1.6(2.0)/\tau) = 0.21(0.05)\%$ of the total background. Adding the two components and including the statistical error and the error on τ , the total amount of hadronic background in the antineutrino candidate sample is $0.18^{+0.09}_{-0.06}$ events.

(ii) *1.6 s cylindrical veto:*

For 27.0% of the muons with a reliably reconstructed track, only a cylinder with 3 m radius is vetoed for 1.6 s. In the [2 ms, 1.6 s] time window after these muons, 7 IBD-like events were observed in the whole detector. Thus, after 1.6 s, we expect $0.015^{+0.013}_{-0.011}$ events distributed in the whole detector. Of these, 2.75% would be reconstructed out of the cylindrical veto, as mentioned before. This means, our expected background of this category can be conservatively set to (0.20 ± 0.08) events. By restricting the veto from the whole detector to only the cylindrical volume, the exposure increases by 1.47%, corresponding to (2.2 ± 0.2) expected IBD events. We observe one additional candidate.

(iii) *2 ms veto of the whole detector:*

For 57.8% of all muons which have a lower probability to produce detectable hadronic background [$(\mu - n)_{<8000}$], we restrict the time veto of the whole detector to 2 ms, to veto only the cosmogenic neutrons. Consequently, the exposure increases by 6.6%, corresponding to (9.7 ± 0.8) expected IBD candidates. Seven candidates were observed, well within the expectation. However, this does not guarantee that we did not introduce additional ${}^9\text{Li}$ background, that is estimated as follows.

Muons with less than 8000 hits produce less light because they pass mostly through the buffer region, where the neutrons are typically not detected or are below the threshold of this analysis. It is reasonable to assume that the production ratios for ${}^9\text{Li}$ and cosmogenic neutrons are the same for $\mu_{<8000}$ and $\mu_{>8000}$ muon categories, since the muons have typically the same energies and the traversed media (LS and the buffer) have nearly the same density. It is also reasonable to assume, that for the $\mu_{<8000}$, the detection efficiency of the corresponding cosmogenic neutrons and neutrons from ${}^9\text{Li}$ decays are the same. Thus,

the equality of the ratios of the number of observed ${}^9\text{Li}$ candidates (with decay neutron, N_{Li}) and cosmogenic neutrons (N_n) should hold:

$$\frac{(N_{\text{Li}}=305)_{>8000}}{(N_n=8.6 \times 10^5)_{>8000}} = \frac{(N_{\text{Li}})_{<8000}}{(N_n=9181)_{<8000}}. \quad (31)$$

From this equality, the expected number $(N_{\text{Li}})_{<8000}$ is 3.2 events. This is the number of expected ${}^9\text{Li}$ events produced by muons with less than 8000 hits, independent of whether this muon was followed by a neutron or not. This is a conservative number for the background estimation due to the $(\mu - n)_{<8000}$ muons, after which we apply the reduced 2 ms cut. Even if they represent about 99% of all $\mu_{<8000}$ muons (Fig. 24), $(\mu + n)_{<8000}$ muons can be expected to have a higher probability to produce observable ${}^9\text{Li}$ than $(\mu - n)_{<8000}$ muons. However, we do not observe any ${}^9\text{Li}$ candidate for $(\mu + n)_{<8000}$ muons. Thus to summarize, our expected ${}^9\text{Li}$ background for $(\mu - n)_{<8000}$ muons is 3.2 ± 1.0 events, which includes larger systematic error.

In total, after summing all the contributions, the expected ${}^9\text{Li}$ background within our golden IBD candidates is (3.6 ± 1.0) events.

2. Untagged muons

The $(0.0013 \pm 0.0005)\%$ mutual inefficiency of the strict muon flags shown in Sec. III B corresponds to (195 ± 75) undetected muons in the entire dataset. Following the discussion in Sec. VI A, these muons could eventually cause background of three types:

- (i) $\mu + \mu$: Considering the small amount of undetected muons in the entire dataset, the probability that two undetected muons would fall in a $1260 \mu\text{s}$ time window of the delayed coincidence is completely negligible.
- (ii) $\mu + n$: The most dangerous are pairs of buffer muons (possibly fulfilling the Q_p cut) followed by a single neutron (multiple neutrons are removed by the multiplicity cut). The probability that a $(\mu + n)$ pair falls within the IBD selection cuts, evaluated on the subset of MTB muons followed by the $TT128$ trigger dedicated to neutron detection, is found to be $(9.7 \pm 0.003) \times 10^{-5}$. Hence, there will be (0.019 ± 0.007) events of this kind in the IBD sample due to the untagged muons.
- (iii) *Muon daughters*: After 1.497×10^7 internal muons we have observed 305 IBD-like background events in a [2 ms, 1.6 s] time window, that covers 99.02% of IBD-like candidates of the same type. Therefore, after (195 ± 75) undetected muons, we can estimate to have (0.0040 ± 0.0015) IBD-like events created

any time after these muons and falling within the selection cuts.

Summing all the three components, the estimated background originating from untagged muons is (0.023 ± 0.007) events in the IBD sample. We note that this is a very small number.

3. Fast neutrons

As described in Sec. VI A, undetected muons that pass the WT or the surrounding rocks, can produce fast neutrons that can give IBD-like signals. Fast neutrons from cosmic muons were simulated according to the energy spectrum from [126]. We have found that the eventual signal from a scattered proton follows in nanosecond time scale after the neutron production, that is simultaneous with the muon signal. Considering the data structure detailed in Sec. III A, this time range dictates the data selection cuts, as described below, in order to search for fast-neutron related IBD-like signals after the detected external muons pass the WT. Knowing the fraction of these muons creating IBD-like background, we can estimate the fast neutron background from the undetected muons that pass the WT. MC simulations are used to obtain an estimation of fast neutron background due to the muons passing through the surrounding rock and not the detector. Both estimations are given below.

a. Water tank muons.—In this search, the signal in the ID should correspond to a scattered proton, which is not tagged by the muon inner detector flag (IDF). Without the proton signal in the ID, the external muon would be a $TT2$ & $BTB4$ event. The presence of the ID signal can, with lower than 100% efficiency, turn the muon to be a $TT1$ & $BTB4$ event. Therefore, we search for two kinds of coincidences:

- (i) The prompt signal is an internal muon $TT1$ & $BTB4$ that is not tagged by the IDF. The delayed signal is a neutron cluster found in the $TT128$ gate which is opened immediately after the muon.
- (ii) The prompt signal is an external muon $TT2$ & $BTB4$ that has a cluster inside the ID, and is not tagged by the IDF. The delayed signal follows within 2 ms as a pointlike $TT1$ & $BTB0$ event.

This search was done with relaxed energy, dt , and dR cuts, without any DFV or multiplicity cuts. This yielded 25 coincidences of the first kind and 12 coincidences of the second kind. However, only one coincidence satisfied all the geoneutrino selection cuts. The amount of these coincidences in the IBD data sample can be due to muons that go undetected by the OD. The average inefficiency of MTF with respect to the MCF and IDF flag is 0.27%, as shown in Table III. This gives an upper limit of 0.013 IBD-like coincidences at 95% C.L. due to the fast neutrons from undetected muons crossing the WT.

b. Surrounding rocks.—In order to study the fast neutron background due to muons passing through the rocks surrounding the detector, we used the Borexino MC with the initial flux and energy spectrum of neutrons and their angular distributions taken from [126] for the specific case of LNGS. The total statistics of MC-generated neutrons corresponds to 3.3 times the exposure of this analysis. Fast neutrons with energies in diapason 1 MeV–3.5 GeV were simulated on the surface of the Borexino outer water tank. Full simulation with tracking of each scintillation photon was done for the fast neutrons and other particles penetrating inside the ID. Finally, we obtain only one IBD-like event for neutrons from the rock passing the optimized IBD selection cuts, which corresponds to an upper limit of the corresponding background in our geoneutrino analysis of <1.43 events at 95 C.L.

D. Accidental coincidences

In order to evaluate the amount of accidental coincidences in the antineutrino sample, coincidence events were searched for in the off-time interval $dt = [2 \text{ s}, 20 \text{ s}]$ and were then scaled to the $1270 \mu\text{s}$ duration of the geoneutrino selection time window ($dt = [2.5 \mu\text{s}, 12.5 \mu\text{s}] + [20 \mu\text{s}, 1280 \mu\text{s}]$, Sec. VII H). In this scaling, a suppression factor due to the muon veto must be considered, as explained below.

To evaluate the accidental background rate which is not biased by the cosmogenics, it is required not only for the prompt, but also for the delayed not to be preceded by a muon within 2 s. This means, that once the prompt is accepted, there is no preceding muon within 2 s before the prompt. After the prompt, as dt between the prompt and a potential delayed increases, so does the probability that the delayed will be discarded due to the muon falling in between the prompt and the delayed. For time intervals longer than 2 s, this probability becomes constant, because the muon veto is of 2 s. This behavior is illustrated in Fig. 36(a), which shows the time distribution between the prompt and delayed accidental signals in a time window $dt = [2 \text{ ms}, 4 \text{ s}]$. One can see that until 2 s, there is a decrease, while after 2 s the distribution is flat. Note that this plot was constructed with relaxed selection cuts and serves only to demonstrate the suppression factor that depends only on the muon rate r_μ and the muon veto time. The fit function for this distribution in the interval $dt = [2 \text{ ms}, 2 \text{ s}]$ is as follows:

$$r_{acc'} = r_0^{acc'} \cdot \exp(-r_\mu \cdot dt), \quad (32)$$

where $r_0^{acc'}$ would be the rate of accidental background with relaxed cuts and without the muon veto suppression factor. After 2 s, the exponential suppression factor becomes constant and consequently the fit function for $dt > 2 \text{ s}$ acquires a constant form:

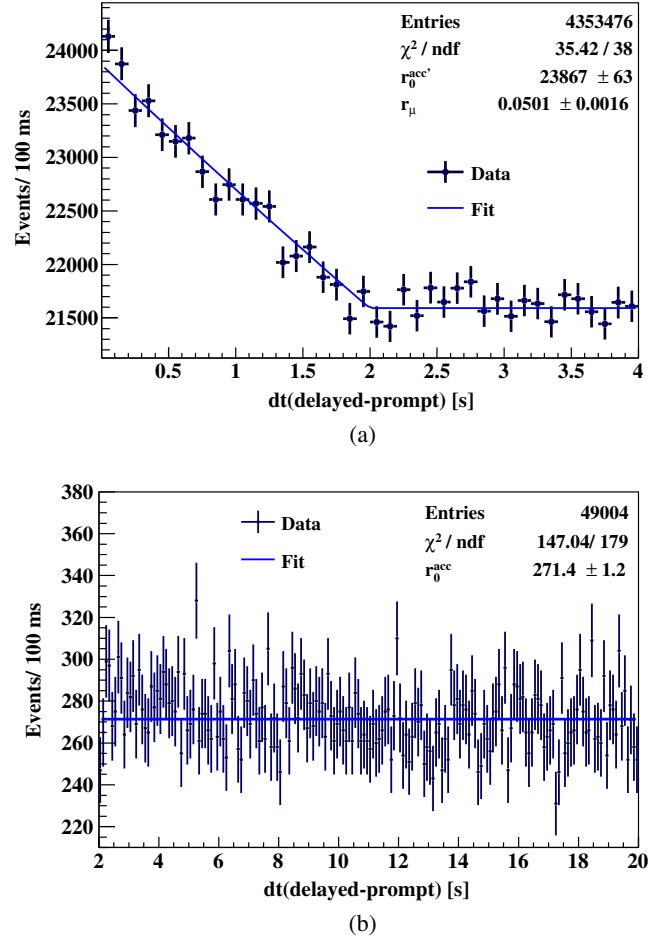


FIG. 36. Distribution of dt (delayed-prompt) for accidental coincidences (a) with relaxed selection cuts to show a decreasing trend until 2 s and a constant trend after 2 s and (b) with geoneutrino selection cuts in the time window $[2 \text{ s}, 20 \text{ s}]$. In both cases the search is performed by applying a 2 s veto for all internal muons.

$$r_{acc'} = r_0^{acc'} \cdot \exp(-r_\mu \cdot 2s). \quad (33)$$

When fitting the spectrum with relaxed cuts, $r_\mu = (0.0501 \pm 0.0016) \text{ s}^{-1}$ was obtained. This is compatible with the measured rate of internal muons of $(0.05311 \pm 0.00001) \text{ s}^{-1}$. The validity of this behavior has been also verified by a MC study.

The suppression factor $\exp(-r_\mu \cdot dt)$ for the dt of the real IBD selection is larger than 0.99993 and thus can be neglected. However, for the times $dt > 2 \text{ s}$, the suppression factor is 0.896 ± 0.003 , conservatively considering also the difference between the r_μ resulting from the fit in Fig. 36(a) and just by measuring the rate of internal muons.

In order to determine the rate of accidental coincidences r_0^{acc} for the geoneutrino measurement, the $dt = [2 \text{ s}, 20 \text{ s}]$ distribution of 49 004 events selected with optimized IBD selection cuts was constructed, as shown in Fig. 36(b). This distribution is, as expected, flat and is fit with a function:

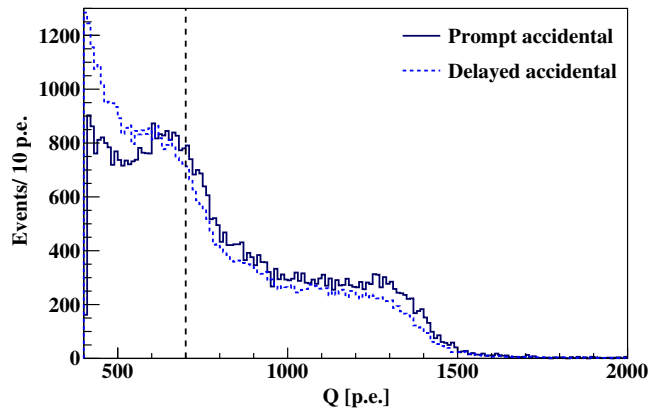


FIG. 37. The charge energy spectrum of the prompts (solid) of accidental coincidences selected in $dt = [2 \text{ s}, 20 \text{ s}]$ time window with the optimized IBD selection cuts. For the delayed signals (dotted), we show the spectrum with Q_d^{\min} lowered to 400 p.e. and scaled to the number of prompts in the solid-line spectrum. The dashed vertical line shows the chosen Q_d^{\min} charge threshold of 700 p.e.

$$r_{\text{acc}} = r_0^{\text{acc}} \cdot \exp(-r_{\mu} \cdot 2s). \quad (34)$$

The exponential suppression factor is set to 0.896 ± 0.003 , the value discussed above, since the muon veto conditions are the same as in the accidental search with relaxed cuts.

The resulting r_0^{acc} is $(3029.0 \pm 12.7) \text{ s}^{-1}$. This means that the number of accidental coincidences among our IBD candidates can be estimated as $r_0^{\text{acc}} \times 1270 \mu\text{s}$, that is (3.846 ± 0.017) events.

The N_{pe} spectra of the prompt and delayed signals of the accidental coincidences, selected with optimized geoneutrino cuts in $dt = [2 \text{ s}, 20 \text{ s}]$ time window, are shown in Fig. 37.

E. (α, n) background

The (α, n) background evaluation is done in three stages. First, the amount of α particles that could initiate this interaction is estimated. In Borexino, the only relevant isotope is ^{210}Po that is found out of equilibrium with the rest of ^{238}U chain [20]. In the energy region of ^{210}Po ($N_{pe} = 150\text{--}300$ p.e.), α -like particles ($MLP < 0.3$) reconstructed in the DFV of the geoneutrino analysis are selected. The evolution of the weekly rates of such events for the whole analyzed period is shown in Fig. 38. The mean rate of $\bar{R}_{\text{DFV}}(^{210}\text{Po}) = (12.75 \pm 0.08) \text{ events}/(\text{day} \cdot \text{ton})$ is used to evaluate the (α, n) background from the ^{210}Po contamination of the LS.

In the second stage, the neutron yield, i.e., the probability that ^{210}Po α would trigger an (α, n) reaction in the LS, was calculated with the NeuCBOT program [127–130], which is based on the TALYS software for simulation of nuclear reactions [122,131,132]. Only PC was considered as a target material. The contribution from PPO is negligible, as

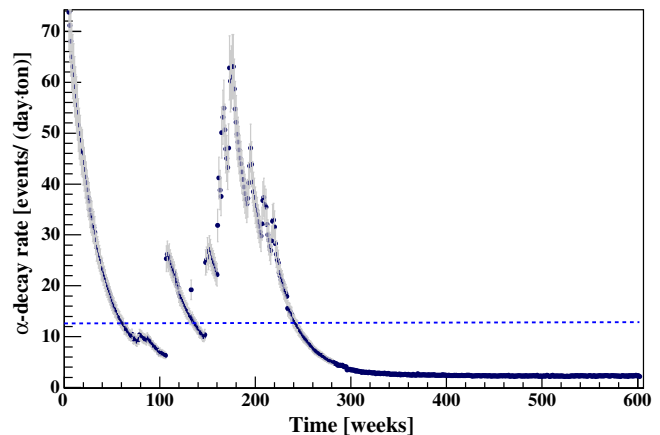


FIG. 38. The evolution of the weekly ^{210}Po α -decay rates in the DFV of geoneutrino analysis, in the period from December 2007 to April 2019. The horizontal line shows the mean rate $\bar{R}_{\text{DFV}}(^{210}\text{Po}) = (12.75 \pm 0.08) \text{ events}/(\text{day} \cdot \text{ton})$.

its relative mass fraction is small. According to a recent article [120], the analytical calculation of the (α, n) cross section with TALYS provides a result similar to the experimental data for energies of the ^{210}Po α particles. This fact permits to apply as a relative uncertainty of our calculation the 15% uncertainty of the experimental data [120]. Taking this into account, the neutron yield Y_n of the (α, n) reaction in the PC is found to be $(1.45 \pm 0.22) \times 10^{-7}$ neutrons per a single ^{210}Po decay. Note that the corresponding value used in the previous Borexino geoneutrino analysis, based on [133], was approximately three times smaller. Even if the (α, n) background is directly proportional to Y_n [see Eq. (35) below], this has a negligible impact on the final geoneutrino result, thanks to a high radio-purity of the Borexino scintillator.

The final calculation of the number of IBD-like coincidences $N_{(\alpha,n)}$ triggered by the neutrons from the (α, n) reaction over the whole analysis period can be computed using the following formula:

$$N_{(\alpha,n)} = \bar{R}_{\text{DFV}}(^{210}\text{Po}) \cdot \mathcal{E} \cdot Y_n \cdot \varepsilon_{(\alpha,n)}, \quad (35)$$

where $\mathcal{E} = (2145.8 \pm 82.1) \text{ ton} \times \text{yr}$ (Sec. IX A) is the exposure and $\varepsilon_{(\alpha,n)} = 56\%$ is the probability of the (α, n) interaction to produce an IBD-like signal passing all selection cuts, obtained with a full $G4Bx2$ MC study. Based on this evaluation, the expected (α, n) background due to the ^{210}Po contamination of the LS is (0.81 ± 0.13) events.

Another potential source of background are (α,n) reactions due to ^{210}Po decays in the buffer. Based on a $G4Bx2$ MC study, we have found that these interactions occurring in the outer buffer have negligible probability to create IBD-like background. However, for the interactions occurring in the inner buffer, this probability was estimated to

be 0.23% and the energy spectrum of prompts is very similar to the (α, n) from the LS (middle panel of Fig. 33). It is extremely difficult to determine the ^{210}Po contamination of the buffer, since the α peak is completely quenched below the detection threshold. In 2009 we have estimated this contamination as <0.67 mBq/kg [16] by employing the samples of buffer liquids in the center of the Counting Test Facility of Borexino [134], that not any more operational. This limit is several orders of magnitude above the contamination of the LS. DMP quencher, that is only present in the buffer, is considered to be the main source of the ^{210}Po contamination in the buffer. In January 2010, the DMP concentration in the buffer was reduced to 2 g/l (the original concentration was 5 g/l), as discussed in Sec. III. Since then, no further operations have been performed with the buffer and the ^{210}Po contamination is expected only to decay ($\tau = 199.6$ day) and to be suppressed in April 2019 by a factor 3.9×10^{-8} . In the present analysis, the estimated upper limit for this contamination is 0.14 mBq/kg, which corresponds to an upper limit of 2.6 background events (from which only 0.3 events in the period from January 2010). We note however, that the original estimate of the ^{210}Po rate in the buffer is very conservative, because of high risk of contamination of the samples during their handling. As it will be discussed in Sec. XI A, the golden IBD candidates are evenly distributed in time and no excess close to the IV is observed.

F. (γ, n) interactions and fission in PMTs

In order to obtain an upper limit to the possible background from (γ, n) reactions in the Borexino scintillator or in surrounding materials, we counted all the registered events with energies higher than 3 MeV and we made the conservative assumption that they are only due to γ -ray interactions. Since the energy response of the detector is not uniform in space and time, an energy release of 3 MeV does not correspond to a unique value of the registered charge N_{pe} . To consider this effect, 3 MeV γ s have been generated with the *G4Bx2* MC code following the detector status during the whole analyzed period. According to Fig. 39, a conservative charge threshold of 1200 p.e. was chosen and a correction of 5.4% for the inefficiency of the cut was then applied: 589 917 events were selected above 1200 p.e., resulting in 623 571 hypothetical γ -rays after the correction. Each of them can only interact with the deuterons that meets along its path before being absorbed: an estimation for this background is then obtained by multiplying the numbers of gammas for the deuteron density, the interaction cross section, and the gamma's absorption length. According to the γ -ray attenuation coefficients calculated for the Borexino scintillator, the absorption length λ for a 3 MeV gamma is 29 cm and the capture cross section on ^2H is $\sigma_D = 1.6$ mb. Since the deuteron density is $\rho_D = 7.8 \times 10^{18}$ atoms/cm³, the upper

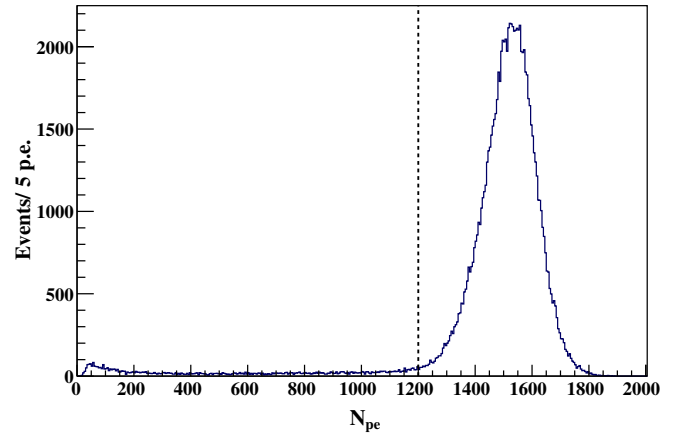


FIG. 39. The N_{pe} distribution of 3 MeV γ s generated in the DFM and in the entire analyzed period of geoneutrino analysis. The vertical line indicates the 1200 p.e. threshold used in the evaluation of the (γ, n) background.

limit on the number of events $N_{(\gamma,n)}$ due to this background, taking into account the estimated detection efficiency $\varepsilon_{(\gamma,n)} = 50\%$, is

$$N_{(\gamma,n)} < N_\gamma \cdot \rho_D \cdot \sigma_D \cdot 3\lambda \cdot \varepsilon_{(\gamma,n)} = 0.34 \text{ events.} \quad (36)$$

An attenuation length of 3λ was chosen to obtain the 95% C.L. A possible contribution of neutron capture on ^{13}C and ^{12}C nuclei was also considered, but it was found to be more than a factor 10 smaller and therefore, neglected.

In PMTs we have determined a ^{238}U contamination of (31 ± 2) ppb in the glass and (60 ± 4) ppb in the dynodes. PMTs are located at about 6.85 m from the center of the detector. To estimate the background induced by spontaneous fission, we consider that for each PMT the glass accounts for about 0.3 kg and the dynodes for 0.05 kg. In addition, we take into account the subtended solid angle by the IV and the neutron attenuation while propagating from the PMTs to the IV, which is of the order of 1 m. The estimated number of neutrons reaching the scintillator is (0.057 ± 0.004) for the current exposure. The corresponding neutron-induced background will be negligibly small and we set for it a conservative upper limit of 0.057 events.

G. Radon background

In Sec. VI E we have discussed how the radon contamination of the LS can induce IBD-like background. Figure 40 demonstrates the increased radon contamination during the WE period. A proper choice of the IBD selection cuts is extremely useful to reduce this kind of background and to safely include the WE period in the geoneutrino analysis.

The energy scale of the $(\alpha + \gamma)$ decays of ^{214}Po (Table XI) was evaluated. The energy scale in *G4Bx2*,

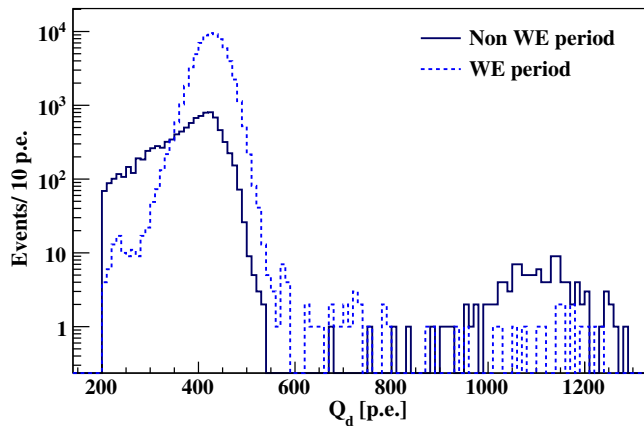


FIG. 40. Charge distribution of delayed signals selected with the low-energy threshold of 200 p.e. and without any MLP cut for the WE period (dotted blue) and the rest of the data-taking (solid blue). The neutron capture peak of the IBDs can be seen at around 1100 p.e. The peak at 400 p.e. is the main α decay of ^{214}Po due to the radon events. The handful of events in between 600 and 860 p.e. are due to the $(\alpha + \gamma)$ decay branch of ^{214}Po , as shown in Table XI.

including the overall light yield and the Birk's constant k_B important in the description of quenching (see Sec. VII of [20]), is tuned based on the calibration with γ sources. Since the k_B is particle dependent, the energy scale for α s must be further adjusted. For this purpose, the dominant pure α decay of ^{214}Po was simulated and compared to the Radon events from the data (selected via the $^{214}\text{Bi};^{214}\text{Po}$ delayed coincidence tag), as demonstrated in Fig. 41(a). With both γ and α energy scales fixed, the spectra for $(\alpha + \gamma)^{214}\text{Po}$ decays were simulated, as it is shown in Fig. 41(b). Since the overall radon statistics amounts to 1.1×10^5 decays, the events due to the 10^{-7} branch can be neglected, while ~ 11 events are expected from the 10^{-4} branch, when ^{214}Po decays to ^{210}Pb in the first excited state. In this case, the deexcitation gamma is emitted along with an α -particle. In order to suppress these events, we keep the Q_d^{\min} threshold fixed to 860 p.e. during the WE period, which effectively reduces this background by a factor of 10^3 . Application of the pulse shape cut (MLP > 0.8) on the delayed (Table XII) further reduces the background by a factor of 5–6. During the analysis of non-WE period, the 10^{-4} branch also becomes negligible, hence we can lower Q_d^{\min} to 700 p.e., safely above the ^{214}Po α -peak [Fig. 41(b)]. The total number of background events correlated with radon contamination is expected to be (0.003 ± 0.001) , which is completely negligible.

H. $^{212}\text{Bi} - ^{212}\text{Po}$ background

A MC study proves that the cut on $Q_d^{\min} = 860$ p.e., adopted to reject the radon contamination during the WE

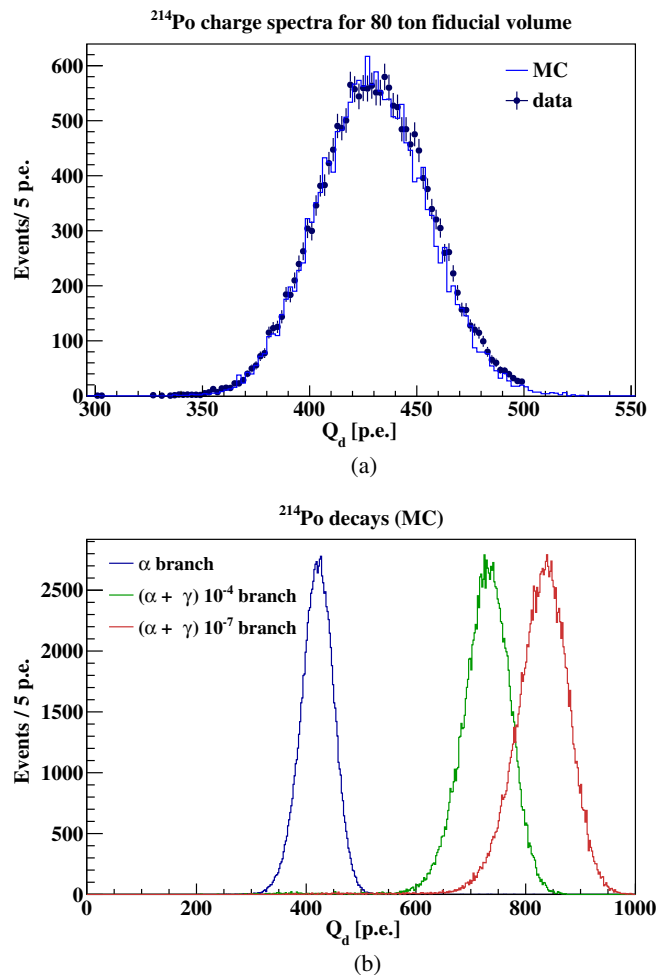


FIG. 41. Top: Comparison of the charge spectra of α decays from ^{214}Po from data (circles with error bars) and MC (solid line) in the fiducial volume of ~ 80 tons around the detector center chosen to tune the alpha particle quenching factor. Bottom: Charge distributions for the three ^{214}Po decays (Table XI) obtained using MC with the α energy scale tuned on pure α -decays [Fig. 41(a)]. The main α decay (red line) and the two subdominant $(\alpha + \gamma)$ branches are shown: 10^{-4} (green line) and 10^{-7} (blue line) branch. The three spectra are normalized to have the same area.

periods, is effective in removing the $^{212}\text{Bi} - ^{212}\text{Po}$ fast coincidences, as shown in Fig. 42. It can be seen that the endpoint of the ^{212}Po α peak is around 700 p.e. Therefore, a Q_d^{\min} of 700 p.e., combined with the MLP pulse shape cut on the delayed, makes the overall $^{212}\text{Bi} - ^{212}\text{Po}$ background fully negligible in geoneutrino analysis.

I. Summary of the estimated nonantineutrino background events

Table XV summarizes the expected number of events from all nonantineutrino backgrounds passing the optimized selection cuts listed in Table XII.

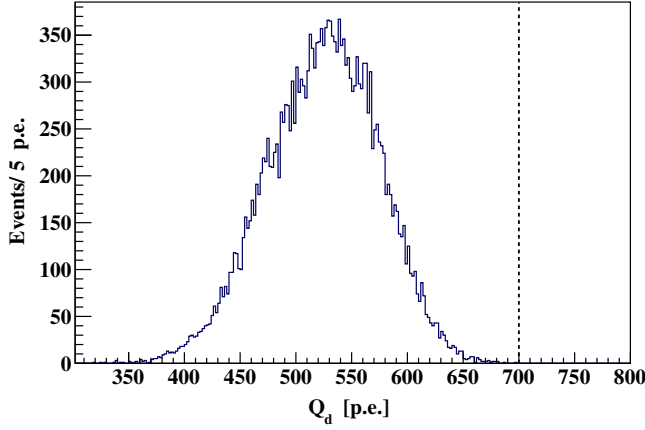


FIG. 42. Charge spectrum of MC generated ^{212}Po α peak. The vertical line at 700 p.e. shows the optimized Q_d^{\min} for IBD selection.

X. SENSITIVITY TO GEONEUTRINOS

This section describes the Borexino sensitivity to geoneutrinos and the MC based procedure with which it was evaluated. In Sec. X A the description of the basic ingredients of the analysis focuses on the spectral fit of the Q_p spectrum. Section X B describes the sensitivity tool that performs such fits on 10 000 Q_p^{MC} spectra, each corresponding to a MC generated pseudoexperiment. The expected precision for the Borexino geoneutrino measurement as well as its sensitivity to the mantle signal is discussed in Sec. X C. This approach was also used in the optimization of the selection cuts, as mentioned in Sec. VII. The systematic uncertainties given in Sec. XI C are not included in the sensitivity studies and are only considered in the final results of Sec. XI. As it will be shown, the error on the geoneutrino measurement is largely dominated by the statistical error.

TABLE XV. Summary of the expected number of events from nonantineutrino backgrounds in the antineutrino candidate sample (exposure $\mathcal{E}_p = (1.29 \pm 0.05) \times 10^{32}$ protons \times yr). The limits are 95% C.L.

Background type	Events
^9Li background	3.6 ± 1.0
Untagged muons	0.023 ± 0.007
Fast n's (μ in WT)	< 0.013
Fast n's (μ in rock)	< 1.43
Accidental coincidences	3.846 ± 0.017
(α , n) in scintillator	0.81 ± 0.13
(α , n) in buffer	< 2.6
(γ , n)	< 0.34
Fission in PMTs	< 0.057
$^{214}\text{Bi} - ^{214}\text{Po}$	0.003 ± 0.001
Total	8.28 ± 1.01

A. Geoneutrino analysis in a nutshell

The geoneutrino signal is extracted from the spectral fit of the charges of the prompts of all selected IBD candidates. Since the number N_{IBD} of selected candidates is relatively small (in this analysis, $N_{\text{IBD}} = 154$ candidates, see Sec. XI A), an unbinned likelihood fit is used:

$$L = (\vec{\theta}; \vec{Q}_p) = \prod_{i=1}^{N_{\text{IBD}}} L(\vec{\theta}; Q_p^i), \quad (37)$$

where \vec{Q}_p is the vector of individual prompt charges Q_p^i , and index i runs from 1 to N_{IBD} . The symbol $\vec{\theta}$ indicates the set of the variables with respect to which the function is maximized, namely the number of events corresponding to individual spectral components with known shapes. In particular, we fit the number of geoneutrino and reactor antineutrino events as well as the number of events from several background components. The shapes of all spectral components are taken from the MC-constructed PDFs (see Figs. 32, 33), with the exception of the accidental background, which can be measured with sufficient precision as shown in Fig. 37 (prompt spectrum). Some of the spectral components are kept free (typically geoneutrinos and reactor antineutrinos), while others (typically other than reactor antineutrino backgrounds) are constrained using additional multiplicative Gaussian pullterms in the likelihood function of Eq. (37).

Naturally, the number of geoneutrinos is always kept free. One way of doing it is by having one free fit parameter for geoneutrinos, when we use the PDF in which the ^{232}Th and ^{238}U contributions are summed and weighted according to the chondritic mass ratio of 3.9, corresponding to R_s signal ratio of 0.27 (Sec. V B). Alternatively, ^{232}Th and ^{238}U contributions can be fit as two independent contributions. Additional combinations are of course possible. For example, in the extraction of the geoneutrino signal from the mantle (Sec. XI E), we constrain the expected lithospheric contribution, while keeping the mantle contribution free.

The number of reactor antineutrino events is typically kept free. It is an important cross-check of our ability to measure electron antineutrinos, when we compare the unconstrained fit results (Sec. XI B 1) with the relatively-well known prediction of reactor antineutrino signal (Sec. V C). In addition, an eventual constraint on reactor antineutrino contribution does not significantly improve the precision of geoneutrinos, as verified and discussed below. The constrained reactor antineutrino signal is however used when extracting the limit on the hypothetical georeactor (Sec. V E), as it will be discussed in Sec. XI G.

Typically, we include the following nonantineutrino backgrounds in the fit: cosmogenic ^9Li , accidental coincidences, and (α , n) interactions. Atmospheric neutrinos are included in the calculation of systematic uncertainties, as it

will be described in Sec. XIC. These background components are constrained in the fit, since independent analyses can yield the well constrained estimates of their rates, as they are summarized in Table XV for nonantineutrino backgrounds and in Table XIV given for atmospheric neutrinos.

B. Sensitivity study

A Monte Carlo approach was used in order to estimate the Borexino sensitivity to geoneutrinos, as well as to optimize the IBD selection cuts (Sec. VII). This so-called *sensitivity study* can be divided in the following four steps:

- (i) The arrays of charges of prompts for signal and backgrounds are generated from the PDFs including the detector response that were either created by the full *G4Bx2* MC code (Sec. VIII A, Figs. 32 and 33) or measured, as for accidental background (Fig. 37, prompt spectrum). For each component, the number of generated charges is given by the expectations, as shown for antineutrino signals in Table XIV and for nonantineutrino backgrounds in Table XV.
- (ii) The generated spectra are fit in the same way as the data (Sec. X A), using in the fit the same PDFs that were used for the generation of these pseudoexperiments. This means, uncertainty due to the shape of the spectral components is not considered. This is justified by the fact, that Borexino's sensitivity to geoneutrinos is by far dominated by the statistical uncertainty.
- (iii) The procedure is repeated 10 000 times for each configuration. In each pseudoexperiment, the number of generated events for signal and all backgrounds is varied according to the statistical uncertainty.
- (iv) The distributions of ratios of the resulting fit value (estimated) over the MC-truth (generated) value in each individual fit are constructed for the parameters of interest. For example, such a distribution for the ratio of the number of geoneutrinos estimated from the fit over the number of generated geoneutrinos should be centered at one (when there is no systematic bias), while the width of this distribution corresponds to the expected statistical uncertainty of the measurement.

C. Expected sensitivity

Using the sensitivity tool as explained in Sec. X B, the expected statistical uncertainty of the Borexino geoneutrino measurement in the presented analysis varies from $(13.76 \pm 0.10)\%$ to $(23.09 \pm 0.17)\%$, depending on the expected signal for different geological models (Table XIV), as demonstrated in Fig. 43. This study assumes the Th/U chondritic ratio to hold. In the previous 2015 Borexino geoneutrino analysis [18], the statistical error was $\sim 26.2\%$.

The sensitivity of Borexino to measure the $^{232}\text{Th}/^{238}\text{U}$ ratio was also studied. As it is shown in Fig. 44, Borexino does not have any sensitivity to determine this ratio. Despite the input ratio assuming the chondritic value (considering the statistical fluctuations), the $^{232}\text{Th}/^{238}\text{U}$ ratio resulting from the fit has nearly a flat distribution for the 10 000 pseudoexperiments. This will be also confirmed by large ^{232}Th versus ^{238}U contours shown in Fig. 48(d) for the fit of the data with free ^{238}U and ^{232}Th components.

The sensitivity of Borexino to measure the mantle signal was studied using the log-likelihood ratio method [135] for the expectations according to four different geological models (CC, GC, GD, and FR, Table XIV). For each geological model, we have generated a set of 10 000 pseudoexperiments with the mantle geoneutrino component included. In addition, we have generated 1.2 million pseudoexperiments without the mantle contribution. In each dataset, we have included the relatively-well known lithospheric contribution (Table VI), as well as the reactor antineutrino “without 5 MeV excess” (Table XIV) and nonantineutrino backgrounds (Table XV).

Each pseudoexperiment from all five datasets (one without the mantle and four with mantle signal according to four geological models), are fit twice: with and without the mantle contribution. The best fit with the mantle contribution fixed to zero corresponds to the likelihood $L\{0\}$. The fit with the mantle component left free results in the likelihood $L\{\mu\}$. Obviously, for the dataset without the mantle being generated, the two likelihoods tend to be the same. For the datasets with the mantle included, the $L\{0\}$ tends to be worse than $L\{\mu\}$: the bigger this difference, the better the sensitivity to observe the mantle signal.

We define the test statistics q ($q \geq 0$):

$$q = -2(\ln L\{0\} - \ln L\{\mu\}), \quad (38)$$

that we call q_0 for the dataset without the mantle generated. The q_0 and the four q distributions for different geological models are shown in Fig. 45. The q_0 corresponds to the theoretical $f(q|0)$ distribution:

$$f(q|0) = \frac{1}{2}\delta(q) + \frac{1}{2\sqrt{2\pi}q} \exp\left(-\frac{1}{2}q\right). \quad (39)$$

The four q distributions we fit with the $f(q|\mu)$

$$f(q|\mu) = \left(1 - \Phi\left(\frac{\mu}{\sigma}\right)\right)\delta(q) + \frac{1}{2\sqrt{2\pi}q} \exp\left(-\frac{1}{2}\left(\sqrt{q} - \frac{\mu}{\sigma}\right)^2\right), \quad (40)$$

where Φ stands for a cumulative Gaussian distribution with mean μ and standard deviation σ . For high statistical

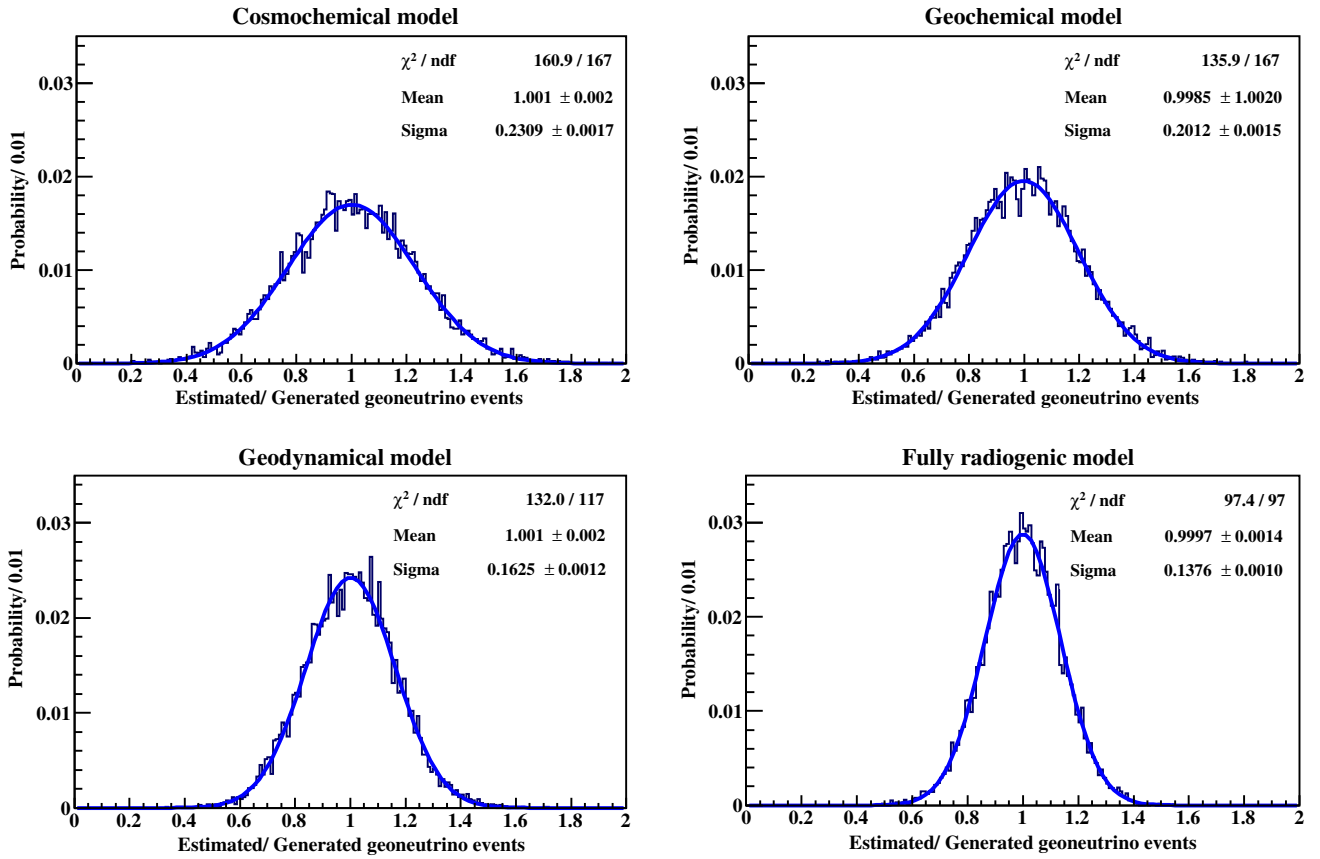


FIG. 43. Results of the sensitivity study for geoneutrinos considering the conditions of the presented analysis: the PDFs for the ratio *Estimated/Generated geoneutrino events* for the CC, GC, GD, and FR Earth models and corresponding fits. Each PDF is based on 10 000 generated spectra. The Gaussian fits are all centered at one, so no systematic bias is expected; their σ 's vary from $(13.76 \pm 0.10)\%$ to $(23.09 \pm 0.17)\%$, depending on the expected geoneutrino signal for different BSE models (Table XIV) and represent the expected statistical uncertainty of the measurement.

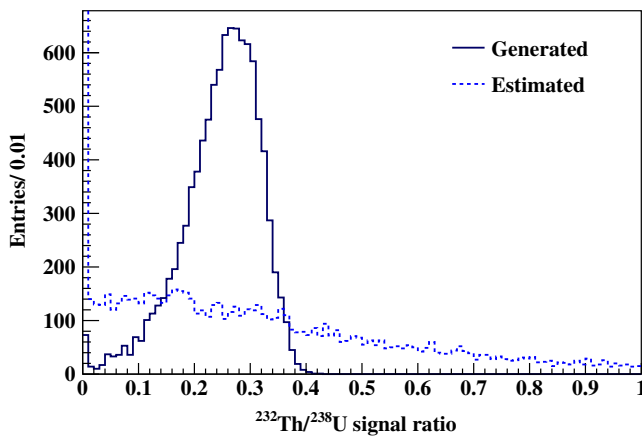


FIG. 44. Demonstration of no sensitivity of Borexino to measure $^{232}\text{Th}/^{238}\text{U}$ geoneutrino signal ratio. Solid line shows the distribution of this ratio, assuming its chondritic value, for 10 000 generated pseudoexperiments. Distribution of this ratio, as obtained from the fit (dotted line), is nearly flat, with a clear peak at 0, due to the ^{232}Th contribution railed to 0.

significance, μ/σ is very large and $\Phi(\frac{\mu}{\sigma}) \rightarrow 1$. In Figure 45 we show also $q_{\text{med}} = (\mu/\sigma)^2$, the median value of $f(q|\mu)$, for the four different geological models. We express the Borexino sensitivity to measure the mantle geoneutrino signal, according to these four geological models, in terms of the p -value, which is given by:

$$p = \int_{q_{\text{med}}}^{\infty} f(q|0). \quad (41)$$

The differences in q_{med} values shown in Fig. 45 for the 4 geological models, that correspond to different p -values and different sensitivity to observe the mantle signal, are to be ascribed only to the differences in the central values of the expected signals (Table XIV), which in turn come from the different central values of U and Th masses associated to the different models (Table VII).

The q_{obs} from the data fit should be used to obtain the final statistical significance of the mantle signal, which will be described in Sec. XI E.

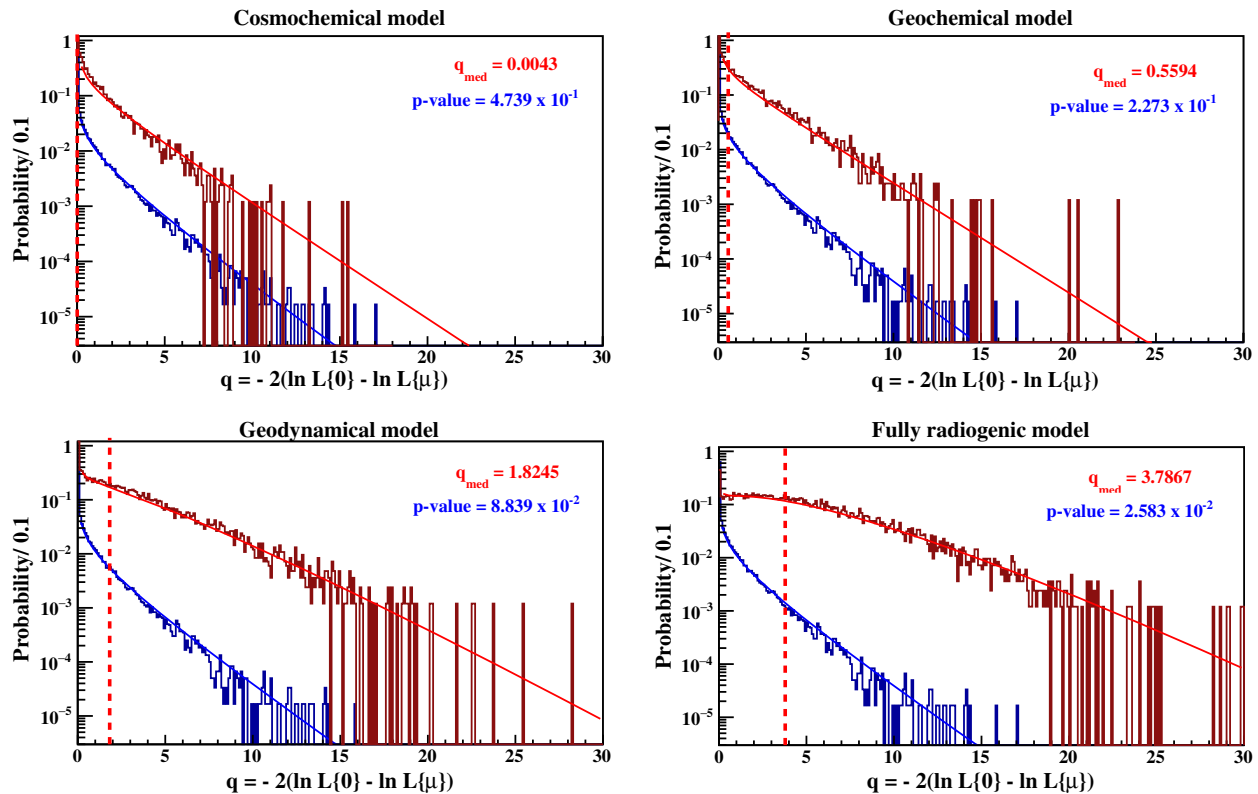


FIG. 45. Distributions of the test statistics $q = -2(\ln L\{0\} - \ln L\{\mu\})$, where $L\{0\}$ and $L\{\mu\}$ are likelihoods of the best fits obtained with the mantle contribution fixed to zero and left free, respectively. Brown solid represents the q values obtained from 10 000 pseudoexperiments with the generated mantle geoneutrino signal, based on the predictions of the different geological models (CC, GC, GD, and FR) and fit with $f(q|\mu)$ according to Eq. (40). The dark blue points show $q = q_0$ test statistics obtained using 1.2M pseudoexperiments without any generated mantle signal and fit with $f(q|0)$ [Eq. (39)]. The vertical dashed lines represent the medians q_{med} of the q distributions. The corresponding p -values are also shown. From the top left to the bottom right panels, the q_{med} values are increasing because of increasing expected mantle signal (i.e., increasing predicted U and Th masses in the mantle).

XI. RESULTS

This section describes the results of our analysis. In Sec. XI A the final IBD candidates selected with the optimized selection cuts are presented. In Sec. XI B the analysis, and in particular the spectral fit with the $^{238}\text{U}/^{232}\text{Th}$ ratio fixed to the chondritic value (Sec. XI B 1) or left free (Sec. XI B 2), is described. The systematic uncertainties are discussed in Sec. XI C. A summary of the geoneutrino signal as measured at the LNGS is given in Sec. XI D. Considering the expected signal from the bulk lithosphere (Table VI), we estimate the geoneutrino signal from the mantle in Sec. XI E. The consequences with regard to the Earth radiogenic heat are then presented in Sec. XI F. Finally, in Sec. XI G the constraints on the power of a hypothetical georeactor (Sec. V E) are set.

A. Golden candidates

In the period between December 9, 2007 and April 28, 2019, corresponding to 3262.74 days of data acquisition, $N_{\text{IBD}} = 154$ golden IBD candidates were observed to pass

the data selection cuts described in Sec. VII. The events are evenly distributed in time [Fig. 46(a)] and radially in the FV [Fig. 46(b)]. The charge distributions of the prompt and delayed signals are also compatible with the expectations, as shown in Figs. 46(c) and 46(d).

The distance to the IV of the prompt signal was also studied. This test would be particularly sensitive to a potential background originated from the IV itself or from the buffer: in the radial distribution of Fig. 46(b), due to the changing IV shape, a small excess of this origin could have been smeared. In fact, in a deformed IV, the points characterized by the same distance from the IV (and thus a potential source of background) can correspond to different radii. As it is shown in Fig. 47, this test was done for all candidates, as well as separately for the geoneutrino energy window (below 1500 p.e.) and above. No excess was observed.

B. Analysis

An unbinned likelihood fit, as described in Sec. X A, was performed with the prompt charge of the 154 golden

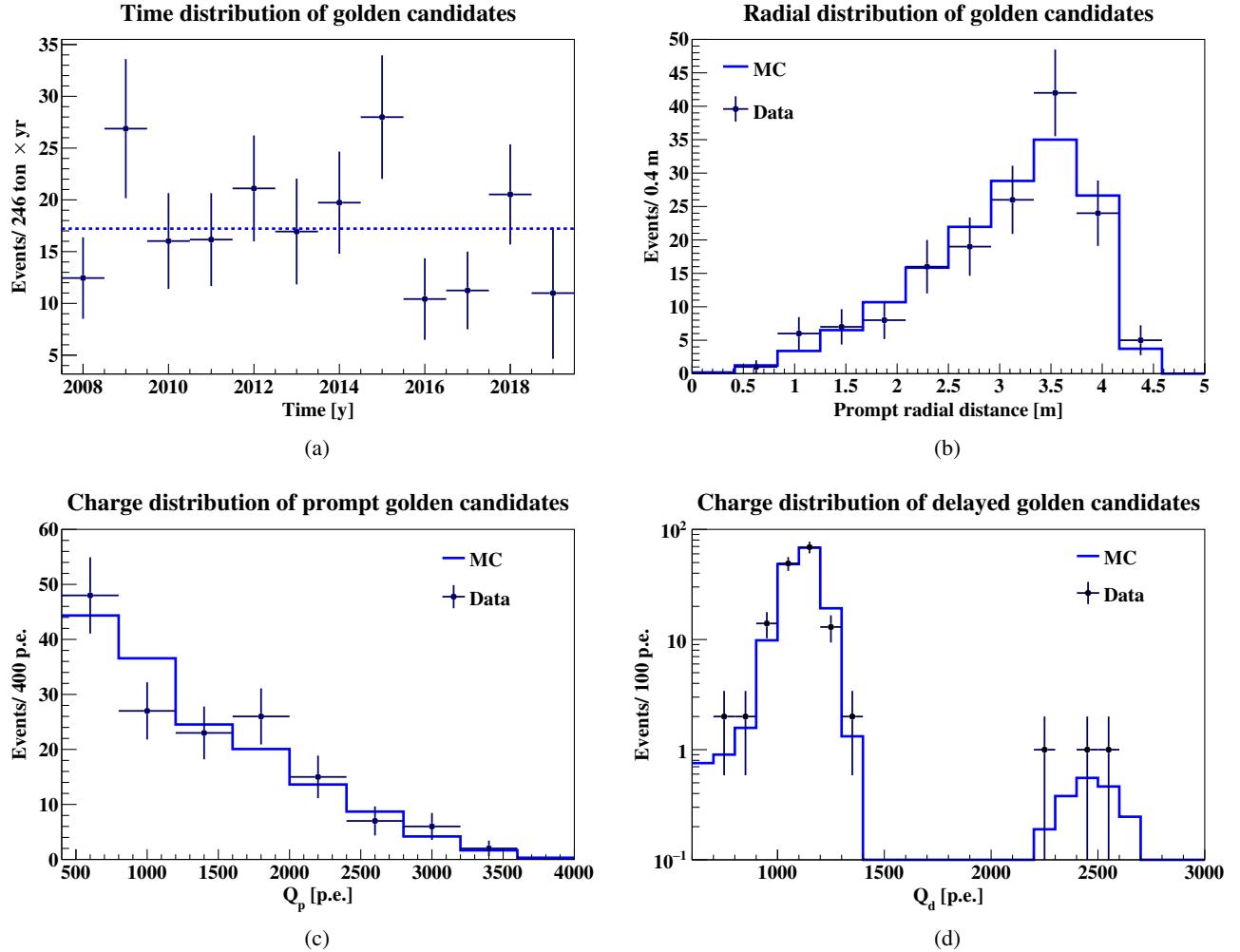


FIG. 46. Distributions for 154 golden IBD candidates (black data points). MC distributions (blue solid lines) are all normalized to the same number of events. (a) Observed IBD-rate (per average FV and one year) as a function of time in one year bins (December 2007 is included in 2008 data point). The dashed line represents the average IBD rate in the entire dataset. (b) Radial distribution of the prompt signals compared to the MC expectation. (c) Charge distribution of the prompts compared to the MC, assuming the geoneutrino and reactor antineutrino events follow the expectations as in Table XIV. (d) Charge distribution of the delayed compared to MC. The two peaks due to the captures on proton and on ^{12}C are clearly visible.

candidates shown in Sec. XI A. The three major non-antineutrino backgrounds, namely, the cosmogenic ^9Li background, the (α, n) background from the scintillator, and accidental coincidences were included in the fit using the PDFs shown in Fig. 33 and Fig. 36(b), respectively. These components were constrained according to values in Table XV with Gaussian pull terms. Reactor antineutrinos were unconstrained in the fit, using the PDF as in Fig. 32(c). The differences in the shape of the reactor antineutrino spectra “with 5 MeV excess” and “without 5 MeV excess” [bottom right in Fig. 32(d)] are included in the systematic uncertainty calculation (Sec. XI C). Obviously, geoneutrinos were also kept unconstrained. The fit was performed in two different ways with respect to the relative ratio of the ^{232}Th and ^{238}U contributions, as detailed in the next two subsections.

The presented fit results are obtained following the recommendations given under the statistics chapter of [136] for cases, when there are physical boundaries on the possible parameter values. In our case, all the fit parameters must have non-negative values. For the main parameters resulting from the fit, the profiles of the likelihood L [Eq. (37)] are provided, and in addition to the best fit values, the mean, median, as well as the 68% and 99.7% coverage intervals for non-negative parameter values, are provided in the summary Table XVII.

1. Th/U fixed to chondritic ratio

The fit was performed assuming the Th/U chondritic ratio and using the corresponding PDF shown in the top-left of Fig. 32(a). The resulting spectral fit is shown in

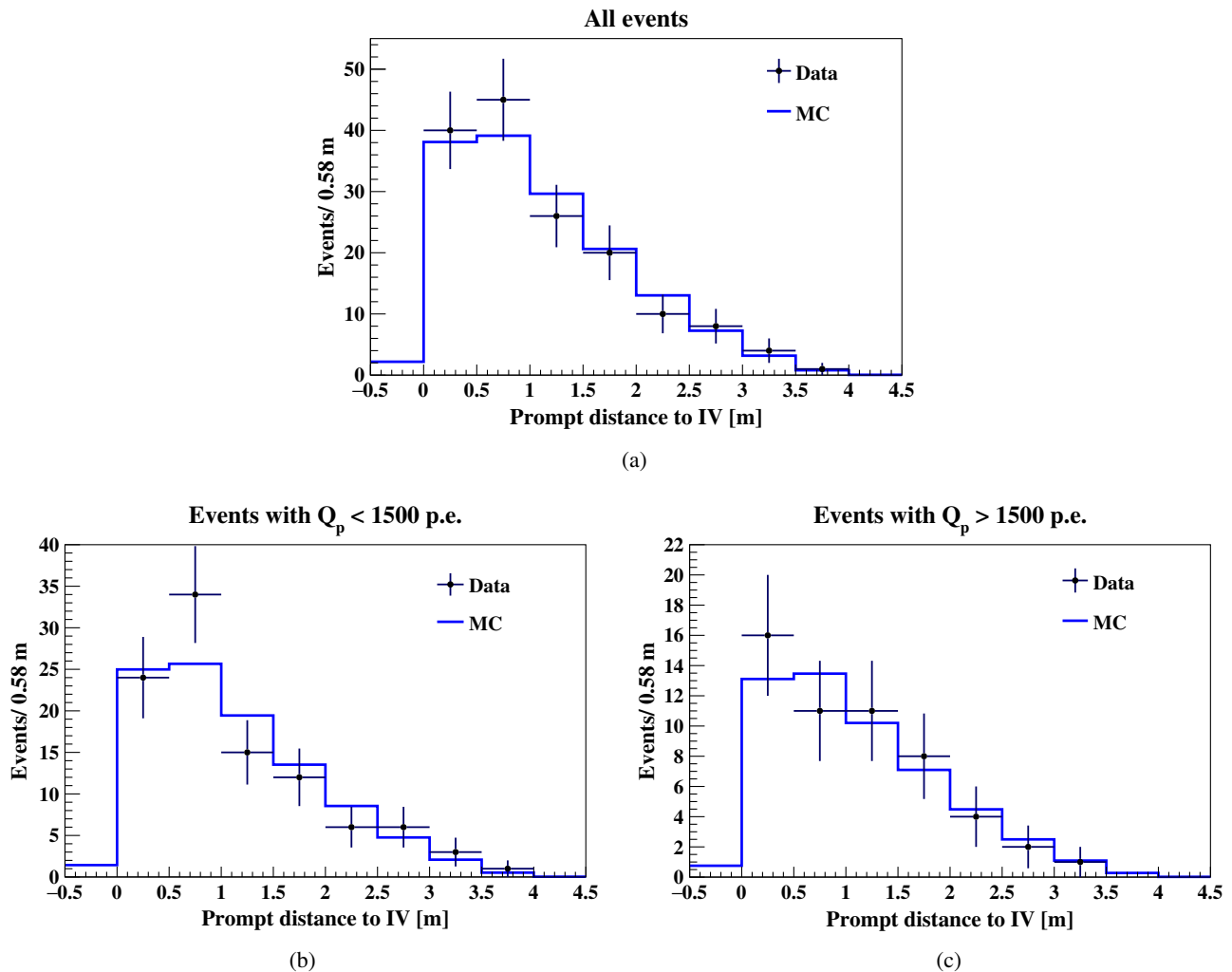


FIG. 47. (a) Prompt's distance to the IV for the 154 golden candidates (black data points) compared to MC (solid blue line) scaled to the same number of events. (b) and (c) show the same distribution but split in two energy windows: below and above the endpoint of the geoneutrinos at 1500 p.e.

Fig. 48(a) and the numerical results are summarized in Table XVII. The likelihood profile for the number of geoneutrinos N_{geo} [Fig. 49(a)], yields the best fit value $N_{\text{geo}}^{\text{best}} = 51.9$, the median value $N_{\text{geo}}^{\text{med}} = 52.6$, and the 68% coverage interval $I_{N_{\text{geo}}}^{68\text{stat}} = [44.0\text{--}62.0]$ events. The likelihood profile for the number of reactor antineutrinos is shown in Fig. 49(b): $N_{\text{rea}}^{\text{best}} = 92.5$ events was obtained with the median value $N_{\text{rea}}^{\text{med}} = 93.4$ and the 68% coverage interval $I_{N_{\text{rea}}}^{68\text{stat}} = [82.6\text{--}104.7]$ events. This is compatible with the reactor antineutrino expectation of (97.6 ± 1.7) events (without “5 MeV excess”) as well as (91.9 ± 1.6) events (with “5 MeV excess”), given in Table XIV. Thus, from the total of 154 golden IBD candidates, the number of detected antineutrinos (geo + reactor) is $N_{\text{antineu}}^{\text{best}} = 144.4$ events. This leaves the number of background events compatible with the expectation (Table XV). The contour plot for N_{geo} versus N_{rea} is shown in Fig. 48(c).

The fit was also performed by constraining the expected number of reactor antineutrino events to (97.6 ± 1.7) events (Table XIV). The result (the best fit value $N_{\text{geo}}^{\text{best}} = 51.3$, the median $N_{\text{geo}}^{\text{med}} = 52.0$, and the 68% coverage interval $I_{N_{\text{geo}}}^{68\text{stat}} = [43.6\text{--}61.1]$ events) is nearly unchanged with respect to that obtained when leaving the reactor antineutrino contribution free. The best fit value is shifted by about 1.5% and the error is only marginally reduced. This fit stability is due to the fact that above the geoneutrino energy window there is almost no non-antineutrino background, and thus the data above the geoneutrino endpoint well constrain the reactor antineutrino contribution also in the geoneutrino window. The fact that without any constraint on N_{rea} the fit returns a value compatible with expectation is an important confirmation of the Borexino ability to measure electron antineutrinos.

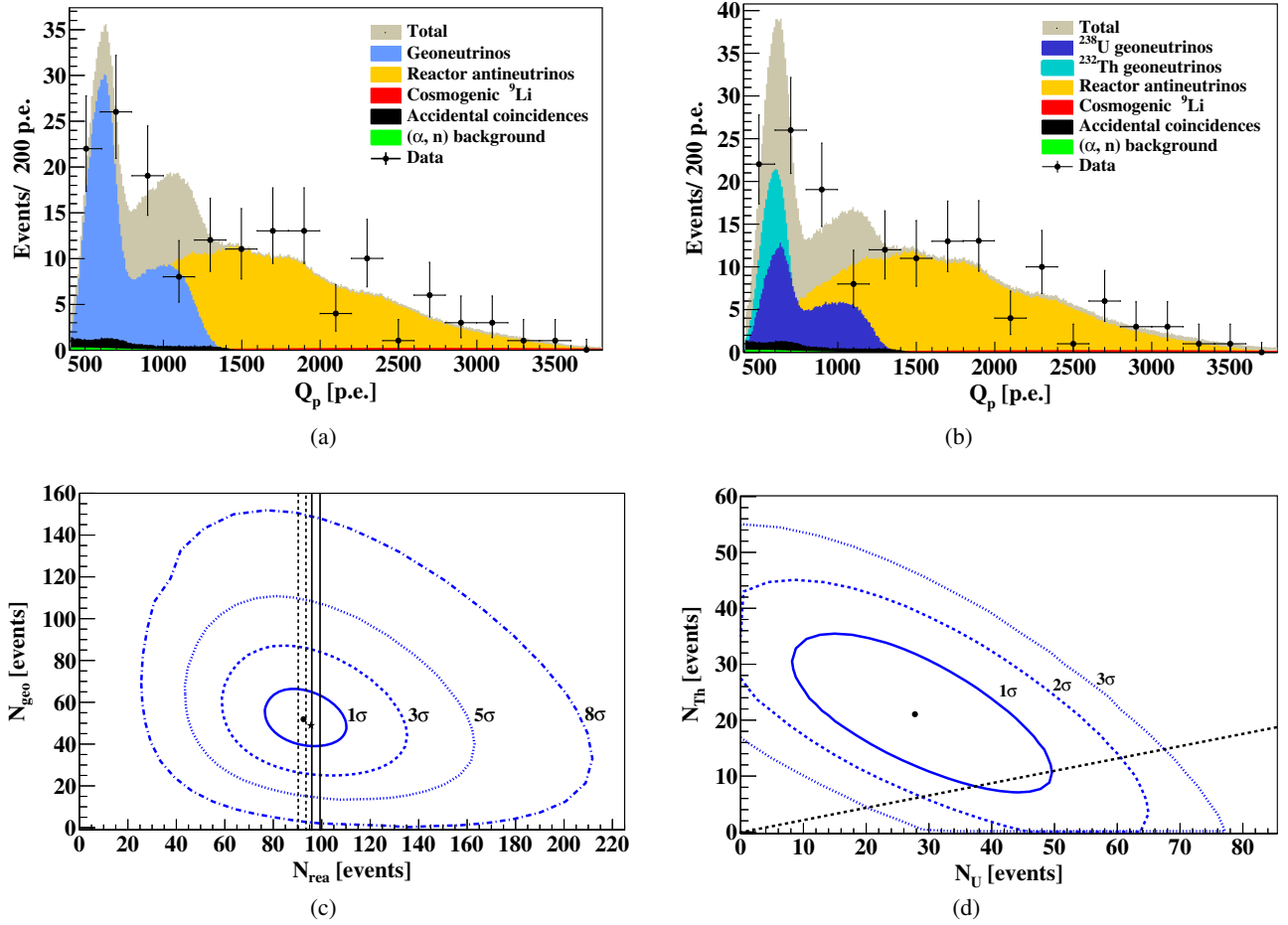


FIG. 48. Results of the analysis of 154 golden IBD candidates. (a) Spectral fit of the data (black points with Poissonian errors) assuming the chondritic Th/U ratio. The total fit function containing all signal and background components is shown in brownish-grey. Geoneutrinos (blue) and reactor antineutrinos (yellow) were kept as free fit parameters. Other nonantineutrino backgrounds were constrained in the fit. (b) Similar fit as in (a) but with ^{238}U (dark blue) and ^{232}Th (cyan) contributions as free and independent fit components. (c) The best fit point (black dot) and the contours for the 2D coverage of 68, 99.7, $(100-5.7 \times 10^{-5})\%$, and $(100-1.2 \times 10^{-13})\%$, (corresponding to 1, 3, 5, and 8σ , respectively), for N_{geo} versus N_{rea} assuming Th/U chondritic ratio. The vertical lines mark the 1σ bands of the expected reactor antineutrino signal (solid—without “5 MeV excess,” dashed—with “5 MeV excess”). For comparison, the star shows the best fit performed assuming the ^{238}U and ^{232}Th contributions as free and independent fit components. (d) The best fit (black dot) and the 68, 95.5, and 99.7% coverage contours (corresponding to 1σ , 2σ , and 3σ contours) N_{Th} versus N_{U} . The dashed line represents the chondritic Th/U ratio.

2. Th and U as free fit parameters

The second type of fit was performed by treating ^{238}U and ^{232}Th contributions as free and independent fit components. The corresponding MC PDFs from Fig. 32(b) were used. The spectral fit is shown in Fig. 48(b) and the numerical results are summarized in Table XVII. The likelihood profiles for the number of ^{238}U and ^{232}Th geoneutrinos are shown in Figs. 49(c) and 49(d), respectively. The fit yielded $N_{\text{U}}^{\text{best}} = 27.8$, $N_{\text{U}}^{\text{med}} = 29.0$, and the 68% coverage interval $I_{N_{\text{U}}}^{68\text{stat}} = [16.1-43.1]$ events for the Uranium contribution and $N_{\text{Th}}^{\text{best}} = 21.1$, $N_{\text{Th}}^{\text{med}} = 21.4$, and the 68% coverage interval $I_{N_{\text{Th}}}^{68\text{stat}} = [12.2-30.8]$ events for the Th contribution. The best fit leads to 48.9 geoneutrinos in total, which is fully compatible with 51.9 geoneutrino

events obtained in the case when Th/U ratio was fixed to the chondritic value. The only difference is significantly larger error in case of the fit with free U and Th contributions. For reactor antineutrinos, $N_{\text{rea}}^{\text{best}} = 95.8$ and $I_{N_{\text{rea}}}^{68\text{stat}} = [85.2-109.0]$ events were obtained, which is also compatible with the expectation. The total number of detected antineutrinos (geo + reactor) is $N_{\text{antineu}}^{\text{best}} = 144.7$ events. The contour plot for N_{geo} versus N_{rea} is shown in Fig. 48(c).

The contour plot for N_{U} versus N_{Th} is shown in Fig. 48(d). The results obtained after constraining the expected N_{rea} were again fully compatible with the results obtained when leaving the reactor antineutrino component free and without any significant reduction on error.

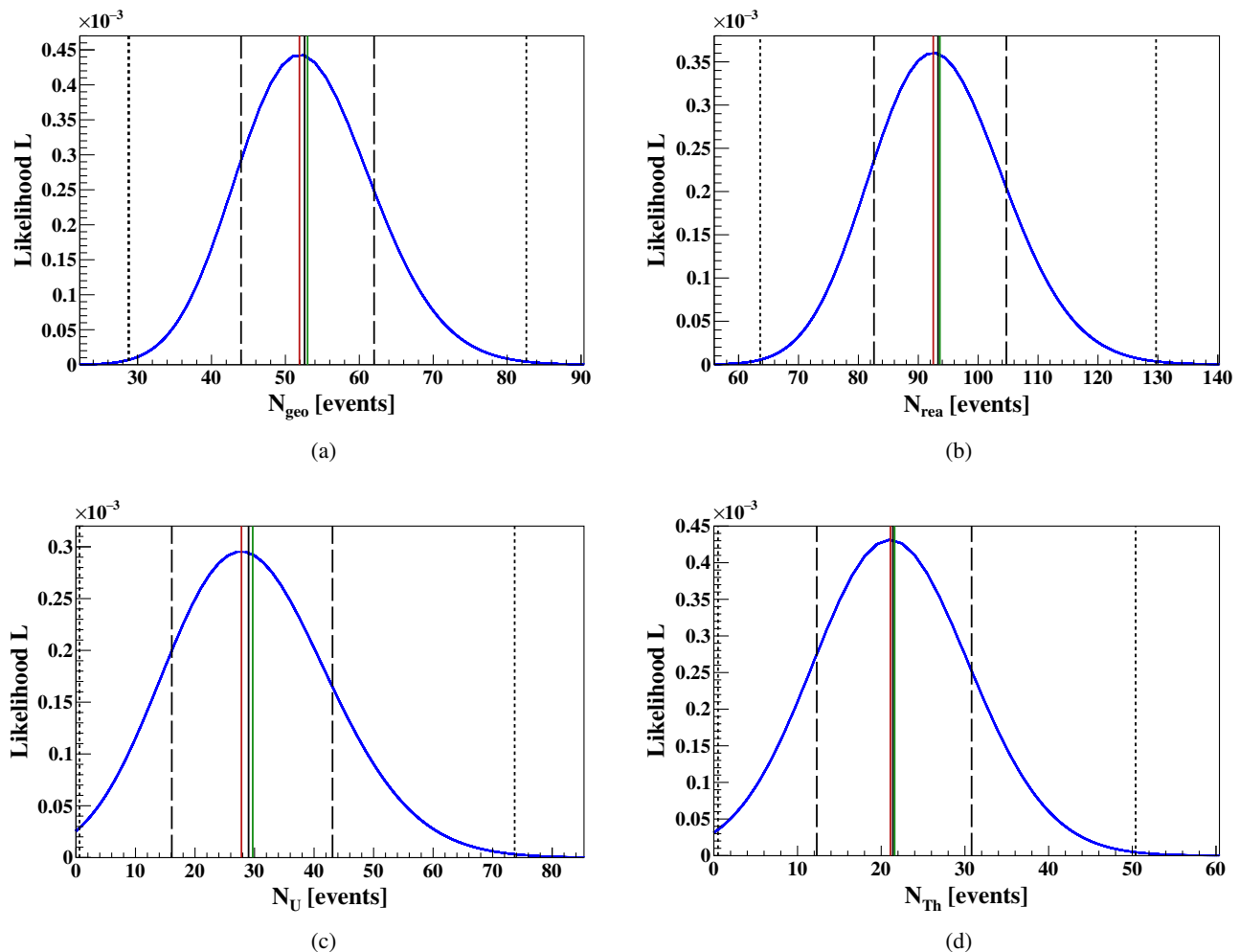


FIG. 49. The likelihood profiles for the number of geoneutrino events N_{geo} (a) and reactor antineutrino events N_{rea} (b) obtained from the fit assuming the chondritic Th/U ratio. The lower row shows the likelihood profiles for the number of ^{238}U (c) and ^{232}Th (d) events obtained from the fit assuming the ^{238}U and ^{232}Th contributions as the two independent free fit components. In each plot, the vertical solid red line indicates the best fit, while the vertical solid black and green lines indicate the median and mean values of the distributions, respectively. The vertical dashed/dotted lines show the 68%/99.7% confidence intervals of the distributions, corresponding to the signal values given in Table XVII.

C. Systematic uncertainties

This section discusses the different sources of systematic uncertainty in the geoneutrino and reactor antineutrino measurement. They are detailed below and summarized in Table XVI.

1. Atmospheric neutrinos

Atmospheric neutrinos as the source of background were discussed in Sec. VD, while the expected number of IBD-like events passing the geoneutrino selection cuts in different energy regions was given in Table XIV. The uncertainty of this prediction is large, estimated to be 50%. In addition, there is an indication of some over-estimation of this background, since above the endpoint of the reactor spectrum, where we would expect (3.3 ± 1.6) atmospheric events, no IBD candidates are observed. In the estimation

of the systematic uncertainty due to atmospheric neutrinos, two fits were performed which were similar to that shown in Fig. 48(a), but with additional contribution due to

TABLE XVI. Summary of the different sources of systematic uncertainty in the geoneutrino and reactor antineutrino measurement. Different contributions are summed up as uncorrelated.

Source	Geo error [%]	Reactor error [%]
Atmospheric neutrinos	+0.00 -0.38	+0.00 -3.90
Shape of reactor spectrum	+0.00 -0.57	+0.04 -0.00
Vessel shape	+3.46 -0.00	+3.25 -0.00
Efficiency	1.5	1.5
Position reconstruction	3.6	3.6
Total	+5.2 -4.0	+5.1 -5.5

atmospheric neutrinos. These are represented by the PDF shown in the top part of Fig. 33. The fit was performed in two energy ranges and the number of events from atmospheric neutrino background was constrained according to the values in Table XIV. First, the fit was performed for data up to the endpoint of the reactor antineutrino spectrum at 4000 p.e., which is the interval containing 63% of atmospheric neutrino background. The resulting number of atmospheric neutrino events is (4.6 ± 3.2) and is compatible with the expectation of (6.7 ± 3.4) . The geoneutrino signal is almost unchanged, while N_{rea} decreased to (89.0 ± 11.3) events. Second, we have performed the fit up to the endpoint of the atmospheric-neutrino background passing our IBD selection criteria (7500 p.e.). In this case, due to the fact that no IBD candidates are observed above the reactor antineutrino energy window, the resulting number of atmospheric neutrino background events is very low and with a large error, (1.2 ± 4.1) events. Fortunately, the resulting N_{geo} and N_{rea} are nearly unchanged. To summarize, we estimate the respective systematic uncertainty on geoneutrinos as $^{+0.00}_{-0.38}$ % and on reactor antineutrinos as $^{+0.00}_{-3.90}$ %.

2. Shape of the reactor spectrum

The likelihood fit, as described in Sec. XIB was performed using the MC PDF of reactor antineutrinos without any “5 MeV excess,” based on the flux prediction of [105], as discussed in Sec. VC. In order to study the changes that might arise due to the observed “5 MeV excess,” the fit was also performed using the corresponding MC PDF as shown in Fig. 32, based on the measured Daya Bay spectrum [101]. Since there is no constraint on N_{rea} and the two spectral shapes are relatively similar, the change in N_{rea} is very small: we observe an increase of 0.05 events. In case of N_{geo} , we observe a decrease of 0.3 events.

3. Inner vessel shape reconstruction

We consider a conservative 5 cm error on the IV position (Sec. III C). This means that the function defining our DFV ($d_{\text{IV}} = 10$ cm) inward from the IV is inside the scintillator with high probability. This implies that the systematic uncertainty on the FV definition due to the IV shape reconstruction is negligible. However, there is a systematic uncertainty due to the selection of the IBD candidates using the DFV cut, which was evaluated by smearing the distance-to-IV of each IBD candidate with a Gaussian function with $\sigma = 5$ cm. Consequently, the DFV cut was applied on the smeared distances and the spectral fit was performed on newly selected candidates. This procedure was repeated 50 times. The distributions of the differences between the resulting N_{geo} and N_{rea} values with respect to the default fit have positive offsets, which were then conservatively taken as the systematic uncertainty due to

the IV shape reconstruction. We estimate the respective systematic uncertainty on geoneutrinos as $^{+3.46}_{-0.00}$ % and on reactor antineutrinos as $^{+3.25}_{-0.00}$ %.

4. MC efficiency

The major source of uncertainty for the MC efficiency arises from the event losses close to the IV edges, especially near the south pole because of the combined effect of a large number of broken PMTs and the IV deformation. The trigger efficiency for the 2.2 MeV gamma from $^{241}\text{Am} - ^9\text{Be}$ calibration source compared to MC simulations for different source positions was studied. The uncertainty in the efficiency was then set to a conservative limit of 1.5%.

5. Position reconstruction

The position of events in Borexino is calculated using the photon arrival times. Since the events are selected inside the DFV based on the reconstructed position, the uncertainty in the position reconstruction of events affects the error on the fiducial volume, and thus, on the resulting exposure. This uncertainty is obtained using the calibration campaign performed in 2009 [76]. Data from the ^{222}Rn and $^{241}\text{Am} - ^9\text{Be}$ sources placed at 182 and 29 positions in the scintillator, respectively, was used for this. The reconstructed position of the source was compared to the nominal source position measured by the CCD camera inside the detector. The uncertainty in position reconstruction for the geoneutrino analysis was calculated using the shift in the positions for the $^{241}\text{Am} - ^9\text{Be}$ source. The maximal resulting uncertainty in the position was observed to be 5 cm. Considering the nominal spherical radius of our FV of 4.15 m, this gives an uncertainty of 3.6% in the fiducial volume and consequently, in the corresponding exposure.

D. Geoneutrino signal at LNGS

This section details the conversion of the number of geoneutrino events N_{geo} , resulting from the spectral fits described in Sec. XIB, to the geoneutrino signal S_{geo} expressed in TNU, the unit introduced in Sec. VB:

$$S_{\text{geo}}[\text{TNU}] = \frac{N_{\text{geo}}}{\epsilon_{\text{geo}} \cdot \frac{\mathcal{E}_p}{10^{32}}} = \frac{N_{\text{geo}}}{\frac{\mathcal{E}'_p}{10^{32}}}, \quad (42)$$

where the detection efficiency $\epsilon_{\text{geo}} = 0.8698 \pm 0.0150$ (Table XIII) and the exposure $\mathcal{E}_p = (1.29 \pm 0.05) \times 10^{32}$ protons \times yr (Sec. III A). We obtain $S_{\text{geo}}^{\text{best}} = 46.3$ TNU, the median value $S_{\text{geo}}^{\text{med}} = 47.0$ TNU, and including the systematic uncertainties from Table XVI, the 68% coverage interval $I_{S_{\text{geo}}}^{68\text{full}} = (38.9 - 55.6)$ TNU. This results in a final precision of our measurement of $^{+18.3}_{-17.2}$ % with respect to $S_{\text{geo}}^{\text{med}}$. The comparison of the result, obtained assuming the

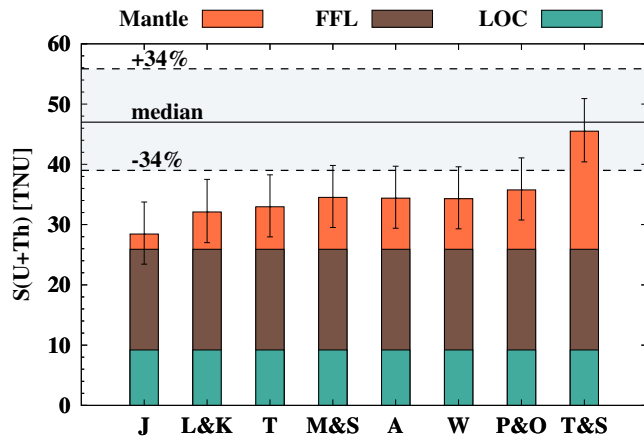


FIG. 50. Comparison of the expected geoneutrino signal $S_{\text{geo}}(U + \text{Th})$ at LNGS (calculated according to different BSE models, see Sec. VB) with the Borexino measurement. For each model, the LOC and FFL contributions are the same (Table VI), while the mantle signal is obtained considering an *intermediate scenario* [Fig. 16(b)]. The error bars represent the 1σ uncertainties of the total signal $S(U + \text{Th})$. The horizontal solid back line represents the geoneutrino signal $S_{\text{geo}}^{\text{med}}$, while the grey band the $I_{S_{\text{geo}}}^{68\text{full}}$ interval as measured by Borexino.

chondritic Th/U mass ratio of 3.9, with the expected geoneutrino signal considering different geological models (Sec. VB) is shown in Fig. 50. Figure 51 shows the time evolution of the Borexino measurements of the geoneutrino signal $S_{\text{geo}}(U + \text{Th})$ at LNGS from 2010 up to the current result. Table XVII summarizes the signals, expressed in TNU, for geoneutrinos and reactor antineutrinos obtained with the two fits, assuming Th/U chondritic ratio and keeping U and Th contributions as free fit parameters, as described in Sec. XIB. It was shown in Sec. XC that Borexino does not have any sensitivity to measure the Th/U ratio with the current

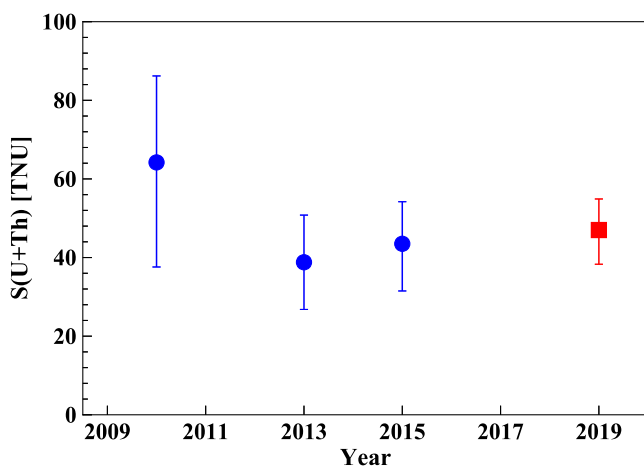


FIG. 51. Comparison of the geoneutrino signal $S_{\text{geo}}(U + \text{Th})$ at LNGS as measured by Borexino. Blue circles indicate the results from 2010 [16], 2013 [17], and 2015 [18], while the red square demonstrates the current analysis.

exposure. Therefore, the ratio obtained from the fit when U and Th are free parameters is not discussed.

E. Extraction of mantle signal

The mantle signal was extracted from the spectral fit by constraining the contribution from the bulk lithosphere according to the expectation discussed in Sec. VB and given in Table XIV as $28.8^{+5.5}_{-4.6}$ events. The corresponding MC PDF was constructed from the PDFs of ^{232}Th and ^{238}U geoneutrinos shown in Fig. 32. They were scaled with the lithospheric Th/U signal ratio equal to 0.29 (Table VI). The MC PDF used for the mantle was also constructed from the ^{232}Th and ^{238}U PDFs, but the applied Th/U signal ratio was 0.26, the value discussed in Sec. VB. The mantle signal, as well as the reactor antineutrino contribution were free in the fit. The best fit is shown in Fig. 52(a). It resulted in a mantle signal of $N_{\text{mantle}}^{\text{best}} = 23.1$ events, with the median value $N_{\text{mantle}}^{\text{med}} = 23.7$ events, and the 68% coverage interval $I_{N_{\text{mantle}}}^{68\text{stat}} = (13.7-34.4)$ events. The likelihood profile of the mantle signal is shown in Fig. 52(b). After considering the systematic uncertainties, the final mantle signal can be given as $S_{\text{mantle}}^{\text{best}} = 20.6$ TNU, with the median value $S_{\text{mantle}}^{\text{med}} = 21.2$ TNU, and the 68% coverage interval $I_{S_{\text{mantle}}}^{68\text{full}} = [12.2-30.8]$ TNU, as shown also in Table XVII.

The statistical significance of the mantle signal was studied using MC pseudoexperiments with and without a generated mantle signal as described in Sec. XC. The q_{obs} obtained from the spectral fit is 5.4479, and it is compared with the theoretical function $f(q|0)$, described in Sec. XC, Eq. (39), as shown in Fig. 53. The corresponding p -value is 9.796×10^{-3} . Therefore, in conclusion the null-hypothesis of the mantle signal can be rejected with 99.0% C.L. (corresponding to 2.3σ significance). The Borexino mantle signal can be compared with calculations according to a wide spectrum of BSE models (Table VII). The Borexino measurement constrains at 90(95)% C.L. a mantle composition with $a_{\text{mantle}}(\text{U}) > 13(9)$ ppb and $a_{\text{mantle}}(\text{Th}) > 48(34)$ ppb assuming for the mantle homogeneous distribution of U and Th and a Th/U mass ratio of 3.7.

F. Estimated radiogenic heat

The global HPEs' masses in the Earth are estimated by matching geophysical, geochemical, and cosmochemical arguments. Direct samplings of the accessible lithosphere constrain the radiogenic heat of $H_{\text{rad}}^{\text{LSp}}(U + \text{Th} + \text{K}) = 8.1^{+1.9}_{-1.4}$ TW (Table V), corresponding to $\sim 17\%$ of the total terrestrial heat power $H_{\text{tot}} = (47 \pm 2)$ TW. The radiogenic heat from the unexplored mantle could embrace a wide range of $H_{\text{rad}}^{\text{mantle}}(U + \text{Th} + \text{K}) = (1.2-39.8)$ TW (Table VII), where the highest values are obtained for a fully radiogenic Earth model.

The total amount of HPEs, as well as their distribution in the deep Earth, affect the geoneutrino flux. We will express

TABLE XVII. Summary of the number of geoneutrino and reactor antineutrino events and the corresponding signals in TNU as well as the fluxes obtained from this work. The systematic uncertainties (Table XVI) are given for the median values.

Criteria	Best fit	Median	Mean	68% C.L. stat.	99.7% C.L. stat.	Sys. error	68% C.L. stat. & sys.
$R_s = S(\text{Th})/S(\text{U}) = 0.27$							
N_{geo} [events]	51.9	52.6	53.0	44.0–62.0	28.8–82.6	+2.7 -2.1	43.6–62.2
N_{rea} [events]	92.5	93.4	93.6	82.6–104.7	63.6–129.7	+4.8 -5.1	81.6–105.8
N_{U} [events]	40.5	41.1	41.4	34.4–48.4	22.5–64.5	+2.1 -1.6	34.0–48.6
N_{Th} [events]	11.4	11.5	11.6	9.7–13.6	6.3–18.1	+0.6 -0.5	9.6–13.7
S_{geo} [TNU]	46.3	47.0	47.3	39.3–55.4	25.7–73.8	+2.4 -1.9	38.9–55.6
S_{rea} [TNU]	79.7	80.5	80.7	71.2–90.3	54.8–111.8	+4.1 -4.4	70.3–91.2
S_{U} [TNU]	35.9	36.3	36.6	30.4–42.8	19.9–57.1	+1.9 -1.5	30.1–43.0
S_{Th} [TNU]	10.4	10.5	10.6	8.7–12.4	5.7–16.5	+0.6 -0.4	8.8–12.6
ϕ_{U} [$10^6 \text{ cm}^{-2} \text{ s}^{-1}$]	2.8	2.8	2.9	2.4–3.4	1.6–4.5	+0.2 -0.1	2.4–3.4
ϕ_{Th} [$10^6 \text{ cm}^{-2} \text{ s}^{-1}$]	2.5	2.6	2.6	2.2–3.0	1.4–4.1	+0.2 -0.1	2.1–3.1
$R_s(\text{lithosphere}) = S(\text{Th})/S(\text{U}) = 0.29; R_s(\text{mantle}) = S(\text{Th})/S(\text{U}) = 0.26$							
N_{mantle} [events]	23.1	23.7	24.1	13.7–34.4	0.6–57.2	+1.2 -1.0	13.6–34.4
S_{mantle} [TNU]	20.6	21.2	21.5	12.2–30.7	0.5–51.1	+1.1 -0.9	12.2–30.8
$S(\text{Th})$ and $S(\text{U})$ independent							
N_{geo} [events]	48.9	50.4	51.3	28.4–73.9	1.1–124.1	+2.6 -2.0	28.2–74.0
N_{rea} [events]	95.8	96.7	97.1	85.2–109.0	65.1–136.1	+4.9 -5.3	84.2–110.1
N_{U} [events]	27.8	29.0	29.7	16.1–43.1	0.6–73.7	+1.5 -1.2	16.0–43.2
N_{Th} [events]	21.1	21.4	21.6	12.3–30.8	0.5–50.4	+1.1 -0.9	12.2–30.8
S_{geo} [TNU]	43.7	45.0	45.8	25.4–66.0	1.0–110.8	+2.3 -1.8	25.2–66.1
S_{rea} [TNU]	82.6	83.4	83.7	73.5–94.0	56.1–117.3	+4.2 -4.6	72.6–94.9
S_{U} [TNU]	24.6	25.7	26.3	14.3–38.1	0.5–65.2	+1.3 -1.0	14.2–38.2
S_{Th} [TNU]	19.2	19.5	19.6	11.2–28.0	0.5–45.8	+1.0 -0.8	11.1–28.0
ϕ_{U} [$10^6 \text{ cm}^{-2} \text{ s}^{-1}$]	1.9	2.0	2.1	1.1–3.0	0.04–5.1	+0.1 -0.1	1.1–3.0
ϕ_{Th} [$10^6 \text{ cm}^{-2} \text{ s}^{-1}$]	4.7	4.8	4.9	2.8–6.9	0.1–11.3	+0.3 -0.2	2.7–6.9

the dependence of the expected mantle geoneutrino signal $S_{\text{mantle}}(\text{U} + \text{Th})$ on the mantle radiogenic power $H_{\text{rad}}^{\text{mantle}}(\text{U} + \text{Th})$. The unequivocal relation between the radiogenic power and the HPEs' masses can be expressed via the constant U and Th specific heats $h(\text{U}) = 98.5 \mu\text{W}/\text{kg}$ and $h(\text{Th}) = 26.3 \mu\text{W}/\text{kg}$ [26]:

$$\begin{aligned}
H_{\text{rad}}^{\text{mantle}}(\text{U} + \text{Th}) &= h(\text{U}) \cdot M_{\text{mantle}}(\text{U}) + h(\text{Th}) \cdot M_{\text{mantle}}(\text{Th}) \\
&= [h(\text{U}) + 3.7 \cdot h(\text{Th})] \cdot M_{\text{mantle}}(\text{U}), \quad (43)
\end{aligned}$$

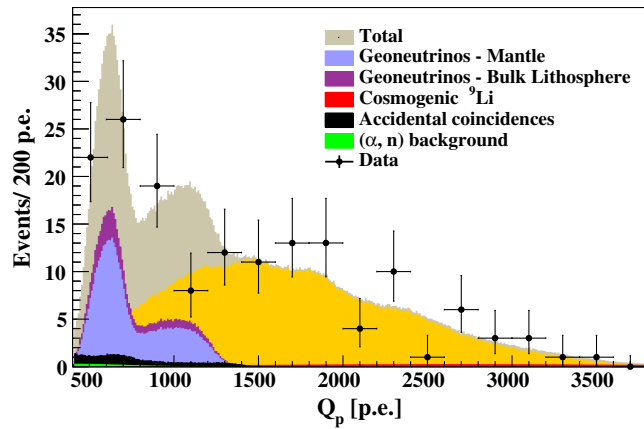
where $M_{\text{mantle}}(\text{U})$ is the U mass in the mantle (Table VII). In the last passage as well as in all calculations below, we assume the mantle Th/U mass ratio of 3.7. With this assumption, for a given detector site the ratio:

$$\beta = S_{\text{mantle}}(\text{U} + \text{Th})/H_{\text{rad}}^{\text{mantle}}(\text{U} + \text{Th}) \quad (44)$$

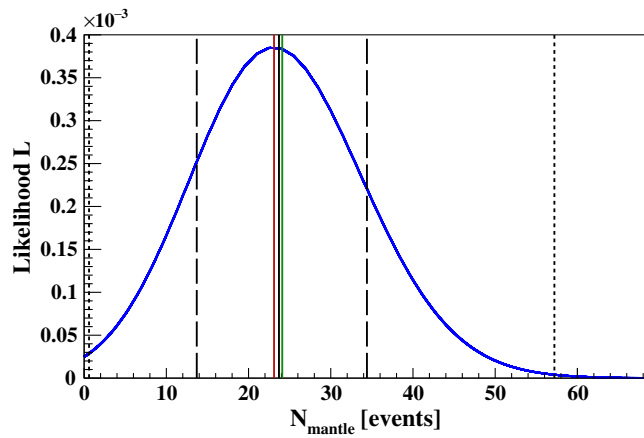
depends only on U and Th distribution in the mantle. For Borexino, the calculated β ranges between $\beta_{\text{low}} = 0.75 \text{ TNU}/\text{TW}$ and $\beta_{\text{high}} = 0.98 \text{ TNU}/\text{TW}$, obtained assuming the HPEs placed in an unique HPEs-rich layer just above the CMB [i.e., low scenario, Fig. 16(a)] and homogeneously distributed in the mantle [high scenario, Fig. 16(c)], respectively. Considering then Eq. (43), the linear relation between the mantle signal $S_{\text{mantle}}(\text{U} + \text{Th})$ and radiogenic power $H_{\text{rad}}^{\text{mantle}}(\text{U} + \text{Th})$ can be expressed:

$$\begin{aligned}
S_{\text{mantle}}(\text{U} + \text{Th}) &= \beta \cdot [h(\text{U}) + 3.7 \cdot h(\text{Th})] \cdot M_{\text{mantle}}(\text{U}) \\
&= \beta \cdot H_{\text{rad}}^{\text{mantle}}(\text{U} + \text{Th}) \quad (45)
\end{aligned}$$

is reported in Fig. 54, where the slope of central line (i.e., $\beta_{\text{centr}} = 0.86 \text{ TNU}/\text{TW}$, black line) is the average of β_{low} (blue line) and β_{high} (red line). The area between the two extreme lines denotes the region allowed by all possible



(a)



(b)

FIG. 52. (a) Spectral fit to extract the mantle signal after constraining the contribution of the bulk lithosphere. The grey shaded area shows the summed PDFs of all the signal and background components. (b) The likelihood profile for N_{mantle} , the number of mantle geoneutrino events. The vertical solid red line indicates the best fit, while the vertical solid black and green lines indicate the median and mean values of the distributions, respectively. The vertical dashed/dotted lines represent the 68%/99.7% confidence intervals of the distribution.

U and Th distributions in the mantle, assuming that the abundances in this reservoir are radial, non-decreasing function of the depth and in a fixed ratio $M_{\text{mantle}}(\text{Th})/M_{\text{mantle}}(\text{U}) = 3.7$. The maximal and minimal excursions of mantle geoneutrino signal is taken as a proxy for the 3σ error range.

Since the radiogenic heat power of the lithosphere is independent from the BSE model, the discrimination capability of Borexino geoneutrino measurement among the different BSE models can be studied in the space $S_{\text{mantle}}(\text{U} + \text{Th})$ vs $H_{\text{rad}}^{\text{mantle}}(\text{U} + \text{Th})$. In Figure 54, the solid black horizontal line represents the Borexino measurement, the median $S_{\text{mantle}}^{\text{med}}$, which falls within prediction of the Geodynamical model (GD). The 68% coverage interval $I_{S_{\text{mantle}}}^{68\text{full}}$, also represented in Fig. 54 by horizontal black

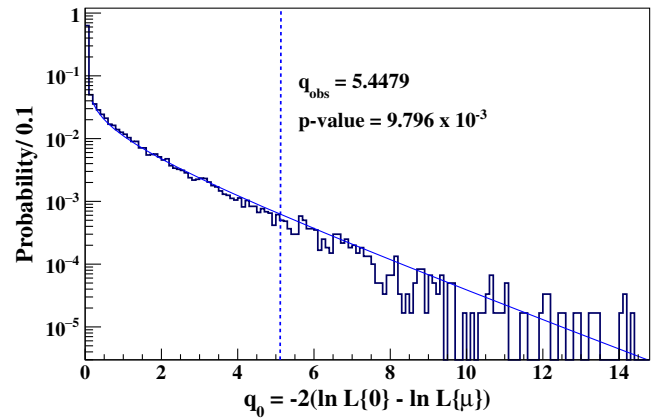


FIG. 53. The q_0 distribution for 1.2 million pseudoexperiments without any generated mantle signal fitted with $f(q|0)$ [Eq. (39)]. The vertical dashed line represents q_{obs} obtained from the data. The indicated p -value, calculated following Eq. (41) by setting $q_{\text{med}} = q_{\text{obs}}$, represents the statistical significance of the Borexino observation of the mantle signal.

dashed lines, covers the area of prediction of the GD and the fully radiogenic (FR) models. We are least compatible with the cosmochemical model (CC), which central value agrees with our measurement at 2.4σ level.

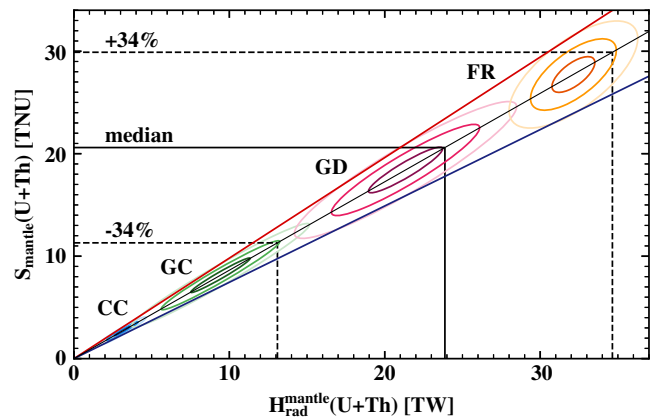


FIG. 54. Mantle geoneutrino signal expected in Borexino as a function of U and Th mantle radiogenic heat: the area between the red and blue lines denotes the full range allowed between a homogeneous mantle [high scenario—Fig. 16(c)] and a unique rich layer just above the CMB [low scenario—Fig. 16(a)]. The slope of the central inclined black line ($\beta_{\text{centr}} = 0.86$ TNU/TW) is the average of the slopes of the blue and red lines. The blue, green, red, and yellow ellipses are calculated with the following U and Th mantle radiogenic power $H_{\text{rad}}^{\text{mantle}}(\text{U} + \text{Th})$ (with 1σ error) according to different BSE models: CC model (3.1 ± 0.5) TW, GC model (9.5 ± 1.9) TW, GD model (21.3 ± 2.4) TW, and FR model (32.2 ± 1.4) TW. For each model darker to lighter shades of respective colors represent 1, 2, and 3σ contours. The black horizontal lines represent the mantle signal measured by Borexino: the median mantle signal (solid line) and the 68% coverage interval (dashed lines).

The mantle signal measured by Borexino can be converted to the corresponding radiogenic heat by inverting the Eq. (45). Since the experimental error on the mantle signal is much larger than the systematic variability associated to the U and Th distribution in the mantle, the radiogenic power from U and Th in the mantle $H_{\text{rad}}^{\text{mantle}}(\text{U} + \text{Th})$ inferred from the Borexino signal $S_{\text{mantle}}(\text{U} + \text{Th})$ can be obtained with:

$$\begin{aligned} H_{\text{rad}}^{\text{mantle}}(\text{U} + \text{Th}) &= (1/\beta_{\text{centr}}) \cdot S_{\text{mantle}}(\text{U} + \text{Th}) \\ &= 1.16 \cdot S_{\text{mantle}}(\text{U} + \text{Th}). \end{aligned} \quad (46)$$

Adopting $S_{\text{mantle}}^{\text{med}}(\text{U} + \text{Th}) = 21.2$ TNU together with the 68% C.L. interval including both statistical and systematic errors (Table XVII), we obtain:

$$\begin{aligned} H_{\text{rad}}^{\text{mantle-med}}(\text{U} + \text{Th}) &= 24.6 \text{ TW} \\ {}^{68\text{full}}_{H_{\text{rad}}^{\text{mantle}}}(\text{U} + \text{Th}) &= 14.2\text{--}35.7 \text{ TW}. \end{aligned} \quad (47)$$

Summing the radiogenic power of U and Th in the lithosphere $H_{\text{rad}}^{\text{LSp}}(\text{U} + \text{Th}) = 6.9^{+1.6}_{-1.2}$ TW, the Earth's radiogenic power from U and Th is $H_{\text{rad}}(\text{U} + \text{Th}) = 31.7^{+14.4}_{-9.2}$ TW.

Assuming the contribution from ^{40}K to be 18% of the total mantle radiogenic heat (Sec. II), the total radiogenic

mantle signal can be expressed as $H_{\text{rad}}^{\text{mantle}}(\text{U} + \text{Th} + \text{K}) = 30.0^{+13.5}_{-12.7}$ TW, where we have expressed the 1σ errors with respect to the median. If we further add the lithospheric contribution $H_{\text{rad}}^{\text{LSp}}(\text{U} + \text{Th} + \text{K}) = 8.1^{+1.9}_{-1.4}$ TW, we get the 68% coverage interval for the Earth's radiogenic heat $H_{\text{rad}}(\text{U} + \text{Th} + \text{K}) = 38.2^{+13.6}_{-12.7}$ TW, as shown in Fig. 55.

The experimental error on the Earth's radiogenic heat power estimated by Borexino is comparable with the spread of power predictions derived from the eight BSE models reported in Table II. This comparison is represented in Fig. 55. Among these, a preference is found for models with relatively high radiogenic power, which correspond to a cool initial environment at early Earth's formation stages and small values of the current heat coming from the secular cooling. However, no model can be excluded at 3σ level.

The total radiogenic heat estimated by Borexino can be used to extract the convective Urey ratio according to Eq. (6). The resulting value of $UR_{\text{CV}} = 0.78^{+0.41}_{-0.28}$ is compared to the UR_{CV} predicted by different BSE models in Fig. 56. The Borexino geoneutrino measurement constrains at 90(95)% C.L. a mantle radiogenic heat power to be $H_{\text{rad}}^{\text{mantle}}(\text{U} + \text{Th}) > 10(7)$ TW and $H_{\text{rad}}^{\text{mantle}}(\text{U} + \text{Th} + \text{K}) > 12.2(8.6)$ TW and the convective Urey ratio $UR_{\text{CV}} > 0.13(0.04)$.

G. Testing the georeactor hypothesis

The georeactor hypothesis described in Sec. VE was tested by performing the spectral fit after constraining the expected number of reactor antineutrino events (Table XIV) to $97.6 \pm 1.7(\text{stat}) \pm 5.2(\text{syst})$. The geoneutrino (Th/U fixed to chondritic mass ratio of 3.9) and georeactor contributions were left free in the fit. For each georeactor

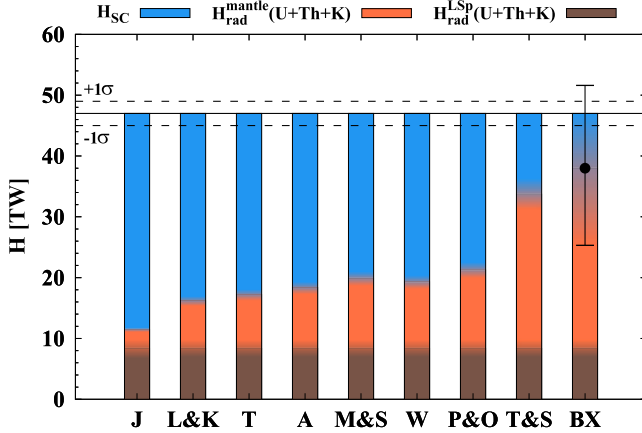


FIG. 55. Decomposition of the Earth's total surface heat flux $H_{\text{tot}} = (47 \pm 2)$ TW (horizontal black lines) into its three major contributions—lithospheric (brown) and mantle (orange) radiogenic heat $H_{\text{rad}}^{\text{LSp}}$ and $H_{\text{rad}}^{\text{mantle}}$, respectively, and secular cooling H_{SC} (blue). The labels on the x axis identify different BSE models (Table VII), while the last bar labeled BX represents the Borexino measurement. The lithospheric contribution $H_{\text{rad}}^{\text{LSp}} = 8.1^{+1.9}_{-1.4}$ TW (Table V) is the same for all bars. The amount of HPEs predicted by BSE models determines the mantle radiogenic heat (Table VII), while for Borexino the value of $30.0^{+13.5}_{-12.7}$ TW is inferred from the extracted mantle signal. The difference between H_{tot} and the respective total radiogenic heat is assigned to the heat from secular cooling of the Earth.

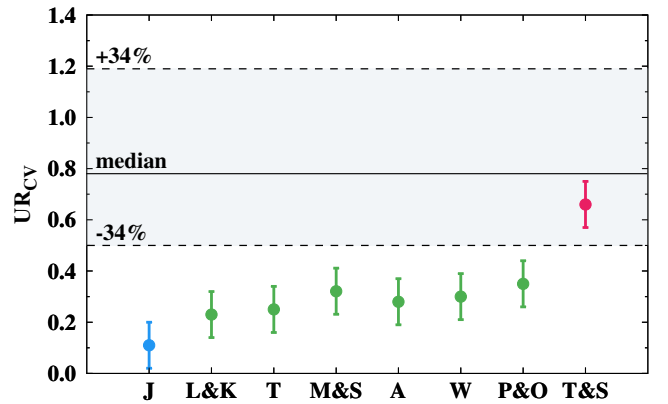


FIG. 56. Comparison of Borexino constraints (horizontal band) with predictions of the BSE models (points with $\pm 3\sigma$ error bars, Table VII) for the convective Urey ratio UR_{CV} [Eq. (6)], assuming the total heat flux $H_{\text{tot}} = (47 \pm 2)$ TW and the radiogenic heat of the continental crust $H_{\text{rad}}^{\text{CC}} = 6.8^{+1.4}_{-1.1}$ TW (Table V). The blue, green, and red colors represent different BSE models (CC, GC, and GD; Table VII, respectively).

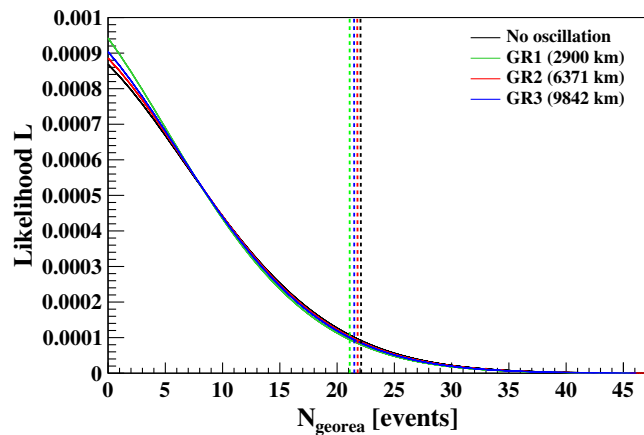


FIG. 57. Likelihood profiles for the number of georeactor events $N_{\text{georeactor}}$ obtained in the spectral fits with the constrained number of reactor antineutrino events. The four profiles represent the fits that differ in the shape of the PDF used for the georeactor contribution (Fig. 34), corresponding to different source positions in the deep Earth [GR1, GR2, GR3, Fig. 21(a)] and to a no-oscillation hypothesis. The vertical dashed lines indicate the upper limit at 95% C.L. for $N_{\text{georeactor}}$ as obtained in each of the four fits. In setting the upper limit on the power of the georeactor, that depends on the assumed location of the georeactor, we use conservatively the highest limit on $N_{\text{georeactor}}$ equal to 21.7 events.

location [Fig. 21(a)], we have used the respective georeactor PDF as in Fig. 34. However, their shapes are practically identical and Borexino does not have any sensitivity to distinguish them. The different likelihood profiles obtained using different georeactor PDFs are very similar (including the PDF constructed assuming no neutrino oscillations), as shown in Fig. 57. The vertical lines represent the 95% C.L. limits for the number of georeactor events $N_{\text{georeactor}}$ obtained in fits with different georeactor PDFs. In setting the upper limit on the power of the georeactor, that depends on the assumed location of the georeactor, we use conservatively the highest limit on $N_{\text{georeactor}}$ equal to 21.7 events. The latter is transformed to the signal $S_{\text{georeactor}}$ of 18.7 TNU, as the 95% C.L. upper limit on the signal coming from a hypothetical georeactor.

Considering the values from Table VIII, that is, the predicted georeactor signal expressed in TNU for a 1 TW georeactor in different locations, these upper limits on the georeactor power are set: 2.4 TW for the location in the Earth center (GR2) and 0.5 TW and 5.7 TW for the georeactor placed at the CMB at 2900 km (GR1) and 9842 km (GR3), respectively. Therefore, we exclude the existence of a georeactor with a power greater than 0.5/2.4/5.7 TW at 95% C.L., assuming its location at 2900/6371/9842 km distance from the detector.

XII. CONCLUSION

Borexino is 280-ton liquid scintillator neutrino detector located at Laboratori Nazionali del Gran Sasso (LNGS) in

Italy, and has been acquiring data since 2007. It has proven to be a successful neutrino observatory, which went well beyond its original proposal to observe ^7Be solar neutrinos. In addition to solar neutrino measurements, Borexino has proven to be able to detect also antineutrinos. Radiopurity of the detector, its calibration, stable performance, its relatively large distance to nuclear reactors, as well as depth of the LNGS laboratory to guarantee smallness of cosmogenic background, are the main building blocks for a geoneutrino measurement with systematic uncertainty below 5%.

The focus of the paper is to provide the scientific community with a comprehensive study that combines the expertise of neutrino physicists and geoscientists. The paper provides an in-depth motivation and description of geoneutrino measurement, as well as the geological interpretations of the result. It presents in detail the analysis of 3262.74 days of Borexino data taken between December 2007 and April 2019 and provides, with some assumptions, a measurement of the Uranium and Thorium content of the Earth's mantle and its radiogenic heat.

Borexino detects geoneutrinos from ^{238}U and ^{232}Th through inverse beta decay, in which electron flavour antineutrinos with energies above 1.8 MeV interact with free protons of the LS. The detection efficiency for optimized data selection cuts is $(87.0 \pm 1.5)\%$. This interaction is the only channel presently available for detection of MeV-scale electron antineutrinos. Optimized data selection including an enlarged fiducial volume and a sophisticated cosmogenic veto resulted in an exposure of $(1.29 \pm 0.05) \times 10^{32}$ protons \times year. This represents an increase by a factor of two over the previous Borexino analysis reported in 2015.

The paper documents improved techniques in the in-depth analysis of the Borexino data, and provides future experiments with a description of the substantial effort required to extract geoneutrino signals. We have underlined the importance of muon detection (in particular special categories of muon events that become crucial in low-rate measurements), as well as the α/β pulse shape discrimination techniques. The optimization of data selection cuts, chosen to maximize Borexino's sensitivity to measure geoneutrinos, has been described. All kinds of background types considered important for geoneutrino measurement have also been discussed, including approaches of their estimation either through theoretical calculation and Monte Carlo simulation, or by analysis of independent data. Borexino ability to measure electron antineutrinos is calibrated via reactor antineutrino background, that is not constrained in geoneutrino analysis and has been found to be in agreement with the expectations. By observing $52.6_{-8.6}^{+9.4}(\text{stat})_{-2.1}^{+2.7}(\text{sys})$ geoneutrinos (68% interval) from ^{238}U and ^{232}Th , a geoneutrino signal of $47.0_{-7.7}^{+8.4}(\text{stat})_{-1.9}^{+2.4}(\text{sys})$ TNU has been obtained. The total precision of $_{-17.2}^{+18.3}\%$ is found to be in agreement with the

expected sensitivity. This result assumes a Th/U mass ratio of 3.9, as found in chondritic CI meteorites, and is compatible with result when contributions from ^{238}U and ^{232}Th were both fit as free parameters.

Importance of the knowledge of abundances and distributions of U and Th in the Earth, and in particular around the detector, for both the signal prediction as well as interpretation of results, have been discussed. The measured geoneutrino signal is found to be in agreement with the predictions of different geological models with a preference for those predicting the highest concentrations of heat producing elements. The hypothesis of observing a null mantle signal has been excluded at 99% C.L. when exploiting detailed knowledge of the local crust near the LNGS. The latter is characterized by the presence of thick, U and Th depleted sediments. We note that geophysical and geochemical observations constrain the Th/U mass ratio for the bulk lithosphere to a value of 4.3. Maintaining the global chondritic ratio of 3.9 for the bulk Earth, the inferred Th/U mass ratio for the mantle is 3.7. Assuming the latter value, we have observed mantle signal of $21.2_{-9.0}^{+9.5}(\text{stat})_{-0.9}^{+1.1}(\text{sys})$ TNU.

Considering different scenarios about the U and Th distribution in the mantle, the measured mantle geoneutrino signal has been converted to radiogenic heat from U and Th in the mantle of $24.6_{-10.4}^{+11.1}$ TW (68% interval). Assuming the contribution of 18% from ^{40}K in the mantle and adding the relatively-well known lithospheric radiogenic heat of $8.1_{-1.4}^{+1.9}$ TW, Borexino has estimated the total radiogenic heat of the Earth to be $38.2_{-12.7}^{+13.6}$ TW. The latter is found to be compatible with different geological predictions. However, there is a $\sim 2.4\sigma$ tension with Earth models predicting the lowest concentration of heat-producing elements. The total radiogenic heat estimated by Borexino can be used to extract a convective Urey ratio of $0.78_{-0.28}^{+0.41}$. In conclusion, Borexino geoneutrino measurement has constrained at 90% C.L. the mantle composition to $a_{\text{mantle}}(\text{U}) > 13$ ppb and $a_{\text{mantle}}(\text{Th}) > 48$ ppb, the mantle radiogenic heat power to $H_{\text{rad}}^{\text{mantle}}(\text{U} + \text{Th}) > 10$ TW and $H_{\text{rad}}^{\text{mantle}}(\text{U} + \text{Th} + \text{K}) > 12.2$ TW, as well as the convective Urey ratio to $UR_{CV} > 0.13$.

With the application of a constraint on the number of expected reactor antineutrino events, Borexino has placed an upper limit on the number of events from a hypothetical georeactor inside the Earth. Assuming the georeactor located at the center of the Earth, its existence with a power greater than 2.4TW has been excluded at 95% C.L.

In conclusion, Borexino confirms the feasibility of geoneutrino measurements as well as the validity of different geological models predicting the U and Th abundances in the Earth. This is an enormous success of both neutrino physics and geosciences. However, in spite of some preference of Borexino results for the models predicting high U and Th abundances, additional and more precise measurements are needed in order to extract firm geological

results. The next generation of large volume liquid scintillator detectors has a strong potential to provide fundamental information about our planet.

ACKNOWLEDGMENTS

The Borexino program is made possible by funding from Istituto Nazionale di Fisica Nucleare (INFN) (Italy), National Science Foundation (NSF) (USA), Deutsche Forschungsgemeinschaft (DFG) and Helmholtz-Gemeinschaft (HGF) (Germany), Russian Foundation for Basic Research (RFBR) (Grants No. 16-29-13014ofi-m, No. 17-02-00305A, and No. 19-02-00097A) and Russian Science Foundation (RSF) (Grant No. 17-12-01009) (Russia), and Narodowe Centrum Nauki (NCN) (Grant No. UMO 2017/26/M/ST2/00915) (Poland). We acknowledge the hospitality and support of the Laboratori Nazionali del Gran Sasso in Italy. The authors thank Matteo Albèri, Cassandra Raptis, and Andrea Serafini for their support.

APPENDIX: LIST OF ACRONYMS

α	Alpha particle
A	BSE model Anderson, 2007 [54]
β	Beta particle
BDT	Boosted decision tree
BSE	Bulk silicate Earth
BTB	Borexino trigger board
BTB4	The same as MTB flag, see below
CC	Continental crust
CC model	Cosmochemical bulk silicate Earth model
C.L.	Confidence level
CLM	Continental lithospheric margin
CMB	Core-mantle boundary
CT	Central Tile
DAQ	Data acquisition
DFV	Dynamical fiducial volume
DM	Depleted mantle
DMP	Dimethylphthalate (DMP, $\text{C}_6\text{H}_4(\text{COOCH}_3)_2$)
e^- or β^-	Electron
e^+ or β^+	Positron
EM	Enriched mantle
E_p	Energy of the prompt IBD candidate
E_d	Energy of the delayed IBD candidate
FADC	Flash analog-to-digital converter
FEB	Front end board
FFL	Far field lithosphere
FR model	Fully radiogenic bulk silicate Earth model
FWFD	Fast wave form digitizer
γ	Gamma ray
G	Gatti parameter
G4Bx2	GEANT4 based Borexino Monte Carlo code
GC model	Geochemical bulk silicate Earth model
GD model	Geodynamical bulk silicate Earth model
GR_1, GR_2, GR_3	3 studied positions of georeactor inside the Earth
H_{rad}	Earth's radiogenic heat

(Table continued)

(Continued)

$H_{\text{rad}}^{\text{CC}}$	Earth's continental crust radiogenic heat
$H_{\text{rad}}^{\text{mantle}}$	Earth's mantle radiogenic heat
$H_{\text{rad}}^{\text{LSp}}$	Earth's lithosphere radiogenic heat
H_{SC}	Earth's heat from the secular cooling
H_{tot}	Integrated total surface heat flux of the Earth
HPEs	Heat producing elements
HSc	High scenario of the mantle signal prediction
IBD	Inverse beta decay
ID	Inner detector
IDF	Inner detector flag
IV	Inner vessel
ISc	Intermediate scenario of the mantle signal prediction
J	BSE model Javoy <i>et al.</i> , 2010 [34]
LF	Load factor of nuclear power plants
L & K	BSE model Lyubetskaya & Korenaga, 2007 [52]
LNGS	Laboratori Nazionali del Gran Sasso
LOC	Local crust
LS	Liquid scintillator
LSc	Low scenario of the mantle signal prediction
LSp	Lithosphere
μ	Muon
MC	Monte Carlo
MLP	Multilayer perceptron
M & S	BSE model McDonough & Sun, 1995 [47]
MTB	Muon trigger board
MTF	Muon trigger flag
m w.e.	Meter water equivalent
ν	Neutrino
$\bar{\nu}$	Antineutrino
$\bar{\nu}_e$	Electron flavor antineutrino
n	Neutron

(Continued)

N_h	Number of detected hits
N_p	Number of triggered PMTs
N_{pe}	Number of detected photoelectrons
OC	Oceanic crust
OD	Outer detector
OV	Outer vessel
p	Proton
P_{ee}	Survival probability of electron flavor neutrino
PC	Pseudocumene liquid scintillator, $\text{C}_6\text{H}_3(\text{CH}_3)_3$, 1,2,4-trimethylbenzene
PDF	Probability distribution function
p.e.	Photoelectron(s)
PID	Particle identification
PM	Primitive mantle
PMNS	Pontecorvo–Maki–Nakagawa–Sakata mixing matrix
PMTs	Photomultiplier tubes
PPO	Fluorescent dye, $\text{C}_{15}\text{H}_{11}\text{NO}$, 2,5-diphenyloxazole
P & O	BSE model Palme and O'Neil, 2003 [56]
Q_p	Charge of the prompt IBD candidate
Q_d	Charge of the delayed IBD candidate
RR	Rest of the region
SSS	Stainless steel sphere
SVM	Support vector machine
T	BSE model Taylor, 1980 [53]
TMVA	Toolkit for multivariate data analysis
TNU	Terrestrial neutrino unit
T & S	BSE model Turcotte & Schubert, 2002 [57]
UR_{CV}	Convective Urey ratio
W	BSE model Wang <i>et al.</i> , 2018 [55]
WE	Water extraction procedure of LS-purification
WT	Water tank

(Table continued)

- [1] W. Winter, *Nucl. Phys.* **B908**, 250 (2016).
- [2] A. Donini, S. Palomares-Ruiz, and J. Salvado, *Nat. Phys.* **15**, 37 (2019).
- [3] S. Bourret, J. A. B. Coelho, and V. Van Elewyck (KM3NeT Collaboration), *J. Phys. Conf. Ser.* **888**, 012114 (2017).
- [4] IAEA nuclear data section, IAEA database, <https://www-nds.iaea.org/relnsd/NdsEnsd/QueryForm.html>.
- [5] G. Fiorentini, M. Lissia, and F. Mantovani, *Phys. Rep.* **453**, 117 (2007).
- [6] G. Marx and N. Menyhárd, *Mitt. Sternwárte Budapest* **44**, 1 (1960).
- [7] G. Eder, *Nucl. Phys.* **78**, 657 (1966).
- [8] G. Marx, *Czech. J. Phys. B* **19**, 1471 (1969).
- [9] L. M. Krauss, S. L. Glashow, and D. N. Schramm, *Nature (London)* **310**, 191 (1984).
- [10] C. G. Rothschild, M. C. Chen, and F. P. Calaprice, *Geophys. Res. Lett.* **25**, 1083 (1998).
- [11] R. S. Raghavan, S. Schönert, S. Enomoto, J. Shirai, F. Suekane, and A. Suzuki, *Phys. Rev. Lett.* **80**, 635 (1998).
- [12] T. Araki *et al.*, *Nature (London)* **436**, 499 (2005).
- [13] S. Abe *et al.* (KamLAND Collaboration), *Phys. Rev. Lett.* **100**, 221803 (2008).
- [14] A. Gando *et al.* (KamLAND Collaboration), *Nat. Geosci.* **4**, 647 (2011).
- [15] A. Gando *et al.* (KamLAND Collaboration), *Phys. Rev. D* **88**, 033001 (2013).
- [16] G. Bellini *et al.* (Borexino Collaboration), *Phys. Lett. B* **687**, 299 (2010).
- [17] G. Bellini *et al.* (Borexino Collaboration), *Phys. Lett. B* **722**, 295 (2013).
- [18] M. Agostini *et al.* (Borexino Collaboration), *Phys. Rev. D* **92**, 031101 (2015).
- [19] N. Vinyoles, A. M. Serenelli, F. L. Villante, S. Basu, J. Bergström, M. C. Gonzalez-Garcia, M. Maltoni, C. Peña Garay, and N. Song, *Astrophys. J.* **835**, 202 (2017).
- [20] G. Bellini *et al.* (Borexino Collaboration), *Phys. Rev. D* **89**, 112007 (2014).
- [21] G. Bellini *et al.* (Borexino Collaboration), *Nature (London)* **512**, 383 (2014).

- [22] M. Agostini *et al.* (Borexino Collaboration), *Nature (London)* **562**, 505 (2018).
- [23] M. C. Chen, *Earth Moon Planets* **99**, 221 (2006).
- [24] F. An *et al.* (JUNO Collaboration), *J. Phys. G* **43**, 030401 (2016).
- [25] L. Wan, G. Hussain, Z. Wang, and S. Chen, *Phys. Rev. D* **95**, 053001 (2017).
- [26] S. Dye, *Rev. Geophys.* **50**, RG3007 (2012).
- [27] M. Agostini *et al.* (Borexino Collaboration), *Astropart. Phys.* **97**, 136 (2018).
- [28] R. M. Gaschnig, R. L. Rudnick, W. F. McDonough, A. J. Kaufman, J. Valley, Z. Hu, S. Gao, and M. L. Beck, *Geochim. Cosmochim. Acta* **186**, 316 (2016).
- [29] National Research Council *et al.*, *Origin and Evolution of Earth: Research Questions for a Changing Planet* (The National Academies Press, Washington, DC, 2008).
- [30] W. F. McDonough, in *Treatise on Geochemistry*, 2nd ed., edited by H. D. Holland and K. K. Turekian (Elsevier, New York, 2014), Vol. 3, pp. 559–577.
- [31] D. C. Rubie, D. J. Frost, U. Mann, Y. Asahara, F. Nimmo, K. Tsuno, P. Kegler, A. Holzheid, and H. Palme, *Earth Planet. Sci. Lett.* **301**, 31 (2011).
- [32] G. Bellini, A. Ianni, L. Ludhova, F. Mantovani, and W. F. McDonough, *Prog. Part. Nucl. Phys.* **73**, 1 (2013).
- [33] A. Deuss and J. Woodhouse, *Science* **294**, 354 (2001).
- [34] M. Javoy *et al.*, *Earth Planet. Sci. Lett.* **293**, 259 (2010).
- [35] Y. Huang, V. Chubakov, F. Mantovani, R. L. Rudnick, and W. F. McDonough, *Geochem. Geophys. Geosyst.* **14**, 2003 (2013).
- [36] N. A. Simmons, A. M. Forte, L. Boschi, and S. P. Grand, *J. Geophys. Res.* **115**, B12310 (2010).
- [37] J. Korenaga, *Rev. Geophys.* **46** (2008).
- [38] C. Jaupart, S. Labrosse, F. Lucazeau, and J. C. Mareschal, in *Treatise on Geophysics*, Vol. 7, edited by G. Schubert (Elsevier B.V., New York, 2015), pp. 223–270.
- [39] A. M. Hofmeister and R. E. Criss, *Tectonophysics* **395**, 159 (2005).
- [40] A. G. Crosby, D. McKenzie, and J. G. Sclater, *Geophys. J. Int.* **166**, 553 (2006).
- [41] C. Jaupart and J. C. Mareschal, in *Treatise on Geophysics*, edited by G. Schubert (Elsevier B.V., New York, 2007), Vol. 6, pp. 217–251.
- [42] J. H. Davies and D. R. Davies, *Solid Earth* **1**, 5 (2010).
- [43] D. L. Williams and R. P. Von Herzen, *Geology* **2**, 327 (1974).
- [44] G. F. Davies, *Rev. Geophys.* **18**, 718 (1980).
- [45] J. G. Sclater, C. Jaupart, and D. Galson, *Rev. Geophys.* **18**, 269 (1980).
- [46] H. N. Pollack, S. J. Hurter, and J. R. Johnson, *Rev. Geophys.* **31**, 267 (1993).
- [47] W. F. McDonough and S. Sun, *Chem. Geol.* **120**, 223 (1995).
- [48] A. Bouvier and M. Boyet, *Nature (London)* **537**, 399 (2016).
- [49] A. Wohlers and B. J. Wood, *Geochim. Cosmochim. Acta* **205**, 226 (2017).
- [50] I. Blanchard, J. Siebert, S. Borensztajn, and J. Badro, *Geochem. Perspect. Lett.* **5**, 1 (2017).
- [51] B. A. Chidester, Z. Rahman, K. Righter, and A. J. Campbell, *Geochim. Cosmochim. Acta* **199**, 1 (2017).
- [52] T. Lyubetskaya and J. Korenaga, *J. Geophys. Res.* **112**, B03212 (2007).
- [53] S. Taylor, *Proc. Lunar Planet. Sci. Conf.* **11**, 333 (1980).
- [54] D. L. Anderson, *New Theory of the Earth*, 2nd ed. (Cambridge University Press, Cambridge, England, 2007).
- [55] H. S. Wang, C. H. Lineweaver, and T. R. Ireland, *Icarus* **299**, 460 (2018).
- [56] H. Palme and H. O'Neill, in *Treatise on Geochemistry*, edited by H. D. Holland and K. K. Turekian (Elsevier, New York, 2003), Vol. 2, pp. 1–38.
- [57] D. L. Turcotte and G. Schubert, *Geodynamics, Applications of Continuum Physics to Geological Problems*, 2nd ed. (Cambridge University Press, Cambridge, England, 2002).
- [58] O. Šrámek, W. F. McDonough, E. S. Kite, V. Lekić, S. T. Dye, and S. Zhong, *Earth Planet. Sci. Lett.* **361**, 356 (2013).
- [59] F. Mantovani, L. Carmignani, G. Fiorentini, and M. Lissia, *Phys. Rev. D* **69**, 013001 (2004).
- [60] R. Arevalo, W. F. McDonough, and M. Luong, *Earth Planet. Sci. Lett.* **278**, 361 (2009).
- [61] J. Blichert-Toft, B. Zanda, D. S. Ebel, and F. Albarède, *Earth Planet. Sci. Lett.* **300**, 152 (2010).
- [62] S. A. Wipperfurth, M. Guo, O. Šrámek, and W. F. McDonough, *Earth Planet. Sci. Lett.* **498**, 196 (2018).
- [63] V. Strati, S. A. Wipperfurth, M. Baldoncini, W. F. McDonough, and F. Mantovani, *Geochem. Geophys. Geosyst.* **18**, 4326 (2017).
- [64] Y. Huang, V. Strati, F. Mantovani, S. B. Shirey, and W. F. McDonough, *Geochem. Geophys. Geosyst.* **15**, 3925 (2014).
- [65] M. Coltorti *et al.*, *Geochim. Cosmochim. Acta* **75**, 2271 (2011).
- [66] J. M. Herndon, *J. Geomagn. Geoelectr.* **45**, 423 (1993).
- [67] J. M. Herndon, *Proc. Natl. Acad. Sci. U.S. A.* **93**, 646 (1996).
- [68] V. D. Rusov, V. N. Pavlovich, V. N. Vaschenko, V. A. Tarasov, T. N. Zelentsova, V. N. Bolshakov, D. A. Litvinov, S. I. Kosenko, and O. A. Byegunova, *J. Geophys. Res.* **112**, 203 (2007).
- [69] R. Meijer and W. Westrenen, *South Afr. J. Sci.* **104**, 111 (2008).
- [70] Y. Wang and L. Wen, *J. Geophys. Res.* **109**, B10305 (2004).
- [71] B. Szczerbinska, D. Alyssa, and M. Dongming, *Proc. Sci.* **90**, 13 (2011).
- [72] A. Cabrera *et al.*, [arXiv:1908.02859](https://arxiv.org/abs/1908.02859).
- [73] K. A. Goettel, *Geophys. Surv.* **2**, 369 (1976).
- [74] G. Alimonti *et al.* (Borexino Collaboration), *Nucl. Instrum. Methods Phys. Res., Sect. A* **600**, 568 (2009).
- [75] M. Agostini *et al.* (Borexino Collaboration), *J. Cosmol. Astropart. Phys.* **02** (2019) 046.
- [76] H. Back *et al.* (Borexino Collaboration), *J. Instrum.* **7**, P10018 (2012).
- [77] G. Bellini *et al.* (Borexino Collaboration), *J. Instrum.* **6**, P05005 (2011).
- [78] H. Voss, A. Hocker, J. Stelzer, and F. Tegenfeldt, *Proc. Sci., ACAT2007* (2007) 040.
- [79] C. Cortes and V. Vapnik, *Mach. Learn.* **20**, 273 (1995).
- [80] Y. Freund and R. E. Schapire, *J. Comput. Syst. Sci.* **55**, 119 (1997).
- [81] G. Lukyanchenko, Ph.D. thesis, National Research Center Kurchatov Institute, (in Russian) (2017), <http://www.nrcki.ru/files/pdf/1490777684.pdf>.

- [82] H. Back *et al.* (Borexino Collaboration), *Nucl. Instrum. Methods Phys. Res., Sect. A* **584**, 98 (2008).
- [83] M. Agostini *et al.* (Borexino Collaboration), *Astropart. Phys.* **92**, 21 (2017).
- [84] A. Strumia and F. Vissani, *Phys. Lett. B* **564**, 42 (2003).
- [85] F. Capozzi, E. Lisi, and A. Marrone, *Phys. Rev. D* **89**, 013001 (2014).
- [86] I. Esteban *et al.*, Nufit 3.2, NuFIT website, <http://www.nu-fit.org/?q=node/166> (2018).
- [87] M. Baldoncini, I. Callegari, G. Fiorentini, F. Mantovani, B. Ricci, V. Strati, and G. Xhixha, *Phys. Rev. D* **91**, 065002 (2015).
- [88] A. M. Dziewonski and D. L. Anderson, *Phys. Earth Planet. Interiors* **25**, 297 (1981).
- [89] G. Fiorentini, A. Ianni, G. Korga, M. Lissia, F. Mantovani, L. Miramonti, L. Oberauer, M. Obolensky, O. Smirnov, and Y. Suvorov, *Phys. Rev. C* **81**, 034602 (2010).
- [90] S. Enomoto, Geoneutrino spectrum and luminosity, online version <https://www.awa.tohoku.ac.jp/~sanshiro/research/geoneutrino/spectrum/>.
- [91] *CROP Project: Deep Seismic Exploration of the Central Mediterranean and Italy*, edited by I. Finetti (Elsevier Science, New York, 2005), Vol. 1.
- [92] T. Plank, in *Treatise of Geochemistry*, 2nd ed., edited by H. D. Holland and K. K. Turekian (Elsevier, New York, 2014), Vol. 4, pp. 607–629.
- [93] C. Bassin, G. Laske, and G. Masters, *EOS Trans AGU* **81**, F897 (2000).
- [94] G. Laske, G. Masters, and C. Reif, Crust 2.0. A new global crustal model at 2×2 degrees, CRUST 2.0 website, <https://igppweb.ucsd.edu/~gabi/crust2.html> (2001).
- [95] N. Shapiro and M. Ritzwoller, *Geophys. J. Int.* **151**, 88 (2002).
- [96] M. Reguzzoni and D. Sampietro, *Int. J. Appl. Earth Observ. Geoinf.* **35**, 31 (2015).
- [97] G. Laske and T. Masters, *EOS Trans. AGU* **78**, F483 (1997).
- [98] World Nuclear Association Database, “Reactor database,” Database website, <https://world-nuclear.org/information-library/facts-and-figures/reactor-database.aspx?id=27232> (2015).
- [99] X. B. Ma, W. L. Zhong, L. Z. Wang, Y. X. Chen, and J. Cao, *Phys. Rev. C* **88**, 014605 (2013).
- [100] IAEA, Power reactor information system (PRIS), PRIS webpage, www.iaea.org/pris (2019).
- [101] F. P. An *et al.* (Daya Bay Collaboration), *Phys. Rev. Lett.* **116**, 061801 (2016); **118**, 099902(E) (2017).
- [102] Y. Abe *et al.* (Double Chooz Collaboration), *J. High Energy Phys.* **10** (2014) 086; **02** (2015) 074(E).
- [103] M. Y. Pac (RENO Collaboration), *Proc. Sci., NUFACT2017* (2018) 038 [arXiv:1801.04049].
- [104] K. Siyeon (NEOS Collaboration), *Proc. Sci., ICRC2017* (2018) 1024.
- [105] T. A. Mueller *et al.*, *Phys. Rev. C* **83**, 054615 (2011).
- [106] F. P. An *et al.* (Daya Bay Collaboration), *Phys. Rev. Lett.* **118**, 251801 (2017).
- [107] G. Mention, M. Vivier, J. Gaffiot, T. Lasserre, A. Letourneau, and T. Materna, *Phys. Lett. B* **773**, 307 (2017).
- [108] H. Ejiri, J. Suhonen, and K. Zuber, *Phys. Rep.* **797**, 1 (2019).
- [109] M. Honda, M. S. Athar, T. Kajita, K. Kasahara, and S. Midorikawa, *Phys. Rev. D* **92**, 023004 (2015).
- [110] G. Battistoni, A. Ferrari, T. Montaruli, and P. R. Sala, *Astropart. Phys.* **23**, 526 (2005).
- [111] R. Wendell, Prob3++ software for computing three flavor neutrino oscillation probabilities, Prob3++ website (2012).
- [112] C. Andreopoulos *et al.*, *Nucl. Instrum. Methods Phys. Res., Sect. A* **614**, 87 (2010).
- [113] K. Farley and E. Neroda, *Annu. Rev. Earth Planet Sci.* **26**, 189 (1998).
- [114] S. T. Dye, *Phys. Lett. B* **679**, 15 (2009).
- [115] V. D. Rusov *et al.*, *J. Mod. Phys.* **4**, 528 (2013).
- [116] J. M. Herndon and D. A. Edgerley, arXiv:hep-ph/0501216.
- [117] G. Bellini *et al.* (Borexino Collaboration), *J. Cosmol. Astropart. Phys.* **08** (2013) 049.
- [118] H. de Kerret *et al.* (Double Chooz Collaboration), *J. High Energy Phys.* **11** (2018) 053.
- [119] J. H. Kelley, J. E. Purcell, and C. G. Sheu, *Nucl. Phys.* **A968**, 71 (2017).
- [120] P. Mohr, *Phys. Rev. C* **97**, 064613 (2018).
- [121] S. Harissopoulos, H. W. Becker, J. W. Hammer, A. Lagoyannis, C. Rolfs, and F. Strieder, *Phys. Rev. C* **72**, 062801 (2005).
- [122] A. J. Koning and D. Rochman, *Nucl. Data Sheets* **113**, 2841 (2012).
- [123] G. Bellini *et al.* (Borexino Collaboration), *Eur. Phys. J. A* **49**, 92 (2013).
- [124] P. Vogel and J. F. Beacom, *Phys. Rev. D* **60**, 053003 (1999).
- [125] Y. Prezado *et al.*, *Phys. Lett. B* **618**, 43 (2005).
- [126] D. M. Mei and A. Hime, *Phys. Rev. D* **73**, 053004 (2006).
- [127] S. Westerdale, NeuCBOT (Neutron Calculator Based On TALYS), GitHub, <https://github.com/shawest/neucbot>.
- [128] S. Westerdale and P. D. Meyers, *Nucl. Instrum. Methods Phys. Res., Sect. A* **875**, 57 (2017).
- [129] S. Westerdale (DEAP-3600 Collaboration), *AIP Conf. Proc.* **1921**, 060002 (2018).
- [130] S. S. Westerdale, A study of nuclear recoil backgrounds in Dark Matter detectors, Ph. D. thesis, Princeton University, 2016, online version: <https://doi.org/10.2172/1350520>.
- [131] A. Koning, S. Hilaire, and M. Duijvestijn, Talys-1.9, TALYS website, <http://www.talys.eu/download-talys/>.
- [132] TALYS-1.0 *Proceedings of the International Conference on Nuclear Data for Science and Technology—ND2007*, edited by O. Bersillon, F. Gunsing, E. Bauge, R. Jacqmin, and S. Leray (EDP Sciences, Nice, France, 2008).
- [133] D. W. McKee, J. K. Busenitz, and I. Ostrovskiy, *Nucl. Instrum. Methods Phys. Res., Sect. A* **587**, 272 (2008).
- [134] G. Alimonti *et al.*, *Nucl. Instrum. Methods Phys. Res., Sect. A* **406**, 411 (1998).
- [135] G. Cowan, K. Cranmer, E. Gross, and O. Vitells, *Eur. Phys. J. C* **71**, 1554 (2011); **73**, 2501(E) (2013).
- [136] M. Tanabashi *et al.* (Particle Data Group), *Phys. Rev. D* **98**, 030001 (2018).

Correction: The order of Figures 14 and 15 was presented incorrectly and has been fixed. The previously published Figure 14(a) contained the wrong image and has been set right.